



1 **February 2017 extreme Saharan dust outbreak in the Iberian**
2 **Peninsula: from lidar-derived optical properties to evaluation**
3 **of forecast models**

4

5 Alfonso J. Fernández¹, Michäel Sicard^{2,3}, Maria J. Costa⁴, Juan L. Guerrero-Rascado^{5,6},
6 José L. Gómez-Amo⁷, Francisco Molero¹, Rubén Barragán^{2,3}, Daniele Bortoli⁴, Andrés
7 E. Bedoya-Velásquez^{5,6}, María P. Utrillas⁷, Pedro Salvador¹, María J. Granados-
8 Muñoz², Miguel Potes⁴, Pablo Ortiz-Amezcu^{5,6}, José A. Martínez-Lozano⁷, Begoña
9 Artíñano¹, Constantino Muñoz-Porcar², Rui Salgado⁴, Roberto Román^{5,6}, Francesc
10 Rocadenbosch^{2,3}, Vanda Salgueiro⁴, José A. Benavent-Oltra^{5,6}, Alejandro Rodríguez-
11 Gómez², Lucas Alados-Arboledas^{5,6}, Adolfo Comerón² and Manuel Pujadas¹.

12

13 ¹Dept. of Environment, Research Centre for Energy, Environment and Technology
14 (CIEMAT), Madrid, Spain.

15 ²Dept. of Signal Theory and Communications, CommSensLab, Universitat Politècnica
16 de Catalunya, Barcelona, Spain.

17 ³Ciències i Tecnologies de l'Espai - Centre de Recerca de l'Aeronàutica i de l'Espai /
18 Institut d'Estudis Espacials de Catalunya (CTE-CRAE / IEEC), Universitat Politècnica
19 de Catalunya, Barcelona, Spain

20 ⁴Institute of Earth Sciences and Dept. of Physics, ECT and IIFA, Universidade de
21 Évora, Évora, Portugal.

22 ⁵Dept. of Applied Physics, University of Granada, Granada, Spain.

23 ⁶Andalusian Institute for Earth System Research (IISTA-CEAMA), Granada, Spain.

24 ⁷Dept. of Physics of the Earth and Thermodynamics, University of Valencia, Valencia,
25 Spain.

26

27 Correspondence to: Alfonso Javier Fernández (alfonsoj.fernandez@ciemat.es)

28

29 **Abstract**

30 An unprecedented extreme Saharan dust event was registered in winter time from 20 to
31 23 February 2017 over the Iberian Peninsula (IP). We report on aerosol optical



32 properties observed under this extreme dust outbreak through remote sensing (active
33 and passive) techniques. For that, EARLINET (European Aerosol Research Lidar
34 NETwork) lidar and AERONET (AErosol RObotic NETwork) Sun-photometer Cimel
35 CE 318 measurements are used. The sites considered are: Barcelona (41.38°N, 2.17°E),
36 Burjassot (39.51°N, 0.42°W), Cabo da Roca (38.78°N, 9.50°W), Évora (38.57°N,
37 7.91°W), Granada (37.16°N, 3.61°W) and Madrid (40.45°N, 3.72°W).

38 In general, large aerosol optical depths (AOD) and low Ångström exponents (AE) are
39 observed. An AOD of 2.0 at 675 nm is reached in several stations. Maximum values of
40 AOD₆₇₅ of 2.5 are registered in Évora. During and around the peak of AOD₆₇₅, AEs
41 close to 0 are measured. With regard to vertically-resolved aerosol optical properties,
42 particle backscatter coefficients as high as $1.5 \cdot 10^{-5} \text{ m}^{-1} \text{ sr}^{-1}$ at 355 nm are recorded at
43 every lidar stations. Mean lidar ratios are found in the range 40 - 55 sr at 355 nm and 34
44 - 61 sr at 532 nm during the event inside the dust layer. Mean particle and volume
45 depolarization ratios are found to be very consistent between lidar stations. They range
46 0.19-0.31 and 0.12-0.26 respectively. The optical properties are also found very stable
47 with height in the dust layer. Another remarkable aspect of the event is the limited
48 height of the dust transport which is found between the ground and 5 km. Our
49 vertically-resolved aerosol properties are also used to estimate the performances of two
50 dust models, namely BSC-DREAM8b and NMMB/BSC-Dust, in order to evaluate their
51 forecast skills in such intense dust outbreaks. We found that forecasts provided by the
52 NMMB/BSC-Dust show a better agreement with observations than the ones from BSC-
53 DREAM8b. The BSC-DREAM8b forecasts (24 h) present a large underestimation
54 during the event. No clear degradation of the prognostics is appreciated in 24, 48, 72 h
55 except for the Barcelona station.

56



57 **1 Introduction**

58 Mineral aerosols are usually originated over arid or semiarid regions as a consequence
59 of continuous soil erosion produced by wind and/or torrential rains. The strong warming
60 of desert areas during daytime produces vertical thermal turbulences that can reach
61 altitudes of up to 5000 m, followed by periods of nocturnal stability (Santos, Costa et al.
62 2013). Massive resuspension of huge amounts of mineral aerosols are thus produced
63 and can be transported long distances by different mechanisms. Actually, 40% of
64 aerosol mass emitted into the troposphere is attributed to desert dust and it is considered
65 as the second largest source of natural aerosols (Andreae 1995, Salvador, Alonso-Perez
66 et al. 2014). One of the main desert dust sources is the Sahara desert since it is
67 responsible for more than half of the world atmospheric mineral dust (Prospero, Ginoux
68 et al. 2002, Mahowald, Baker et al. 2005, Wagner, Bortoli et al. 2009, Salvador,
69 Almeida et al. 2016). Under specific synoptic meteorological situations, a large amount
70 of Saharan dust is transported towards the Mediterranean basin (Lafontaine, Bryson et
71 al. 1990, Obregón, Pereira et al. 2015, Cuevas, Gómez-Peláez et al. 2017).

72 Lately, the number of surveys which address the study of atmospheric mineral aerosols
73 has been increased for several reasons. Firstly, from the climate change standpoint,
74 mineral aerosols play an important role on atmospheric radiative budget through
75 scattering and absorption of the incoming solar and outgoing infrared radiation, and
76 acting as cloud condensation nuclei (Ansmann, Mattis et al. 2005, Klein, Nickovic et al.
77 2010, IPCC 2013). Currently, the large temporal and spatial variability is responsible
78 for a high uncertainty degree in aerosol radiative forcing estimates (Boucher, Forster et
79 al. 2013) (Forster, Ramaswamy et al. 2007). Furthermore, there is a lack of systematic
80 statistical surveys during a long time period. Some of them, (Mona, Amodeo et al.
81 2006) (Salvador, Artíñano et al. 2013) (Pey, Querol et al. 2013), have indicated that the



82 Mediterranean basin is affected by African dust outbreaks following a marked seasonal
83 pattern. Clear summer prevalence has been detected in the western side (Sicard,
84 Barragan et al. 2016), no seasonal trend has been observed in the central region and
85 higher contributions of desert dust have been commonly produced in spring-early
86 summer in the eastern side of this basin.

87 Winter is the season when these phenomena are less likely to occur across the whole
88 Mediterranean basin (Querol, Pey et al. 2009). However, extreme dust outbreaks, as the
89 one described in this paper or others that took place quite recently (Cazorla, Casquero-
90 Vera et al. 2017, Sorribas, Adame et al. 2017), occurred during the coldest season. This
91 is important to be highlighted as extreme weather events have been discussed and
92 suggested to be connected to climate change. For instance some remaining questions
93 concern whether or not such events take place earlier or later in the season or if their
94 severity has been increased (World Meteorological Organization 2011).

95 What is more, it has been demonstrated that African dust is the main source contributing
96 to the regional background levels of PM_{10} (particular matter with an aerodynamic
97 diameter lower than $10\ \mu m$) across the Mediterranean (35-50% of PM_{10}) with maximum
98 contributions up to 80% of the total PM_{10} mass (Pey, Querol et al. 2013). These
99 sporadic but intense natural contributions of PM have been responsible of a high
100 number of exceedances of the PM_{10} daily limit value ($50\ \mu g/m^3$, after the 2008/50/EC
101 European Directive) as registered in different rural and urban monitoring sites across the
102 Mediterranean Basin (Querol, Pey et al. 2009, Salvador, Artíñano et al. 2013).
103 Moreover, statistically significant evidences on the association between short-term
104 exposure to desert dust and health outcomes have also been derived. PM_{10} originating
105 from the desert was positively associated with mortality and hospitalizations in 13
106 Southern European cities for the period 2001-2010 (Stafoggia, Zauli-Sajani et al. 2016).



107 A recent regional study carried out in Spain has associated PM₁₀ levels with daily
108 mortality during African dust outbreaks in most of the Spanish regions (Díaz, Linares et
109 al. 2017).

110 In addition, massive aerosol emissions into the atmosphere can be an issue for aircraft
111 operation. For instance, aircraft engines, that fly through atmospheres with significant
112 mineral dust loads on a regular basis, usually undergo an accelerated aging, and as a
113 result, an anticipated and unexpected overhaul and maintenance is required (Weinzierl,
114 Sauer et al. 2012). In addition, atmospheric mineral dust can cause a huge impact on
115 aviation by reducing the visibility during the landing and takeoff of aircrafts (Weinzierl,
116 Ansmann et al. 2017).

117 For all these reasons, characterizing these events in detail is strictly necessary given the
118 aforementioned implications on human society. In this article, we report on a record-
119 breaking dust event that hit the Iberian Peninsula (IP) on 20 - 23 February 2017. The
120 observational task has been carried out through remote sensing techniques at different
121 sites located in the IP. Sun and sky scanning spectral radiometers and lidar
122 measurements have provided observations concerning the spatial (vertical and
123 horizontal) distribution of aerosol. In this sense, the lidar technique is indispensable
124 since it can provide both temporally and vertically resolved dust layering structures. To
125 give an idea of the magnitude of the extreme event it is noteworthy to state that the
126 AOD was greater than 2 at 675 nm in several AERONET stations and for the most
127 intense periods some lidar and sun-photometer retrievals could not be performed due to
128 high aerosol load, respectively, attenuating the lidar signal and blocking the sun. A
129 previous work concerning such event at the IP found an AODs at 500 nm up to 1.5 in
130 the south of Spain (Guerrero-Rascado, Olmo et al. 2009). In this case, maximum values
131 of particle backscatter coefficients ($1.5 \cdot 10^{-5} \text{ m}^{-1} \text{ sr}^{-1}$ at 355 nm) were similar to those



132 registered during this event, however it took place in September. Preissler et al. reported
133 an aerosol optical thickness up to 2 in Portugal as a consequence of another extreme
134 dust outbreak episode (Preissler, Wagner et al. 2011).

135 Finally, having the capability to forecast such events is also very important. Comparison
136 exercises between real and modeled data must be done in order to better comprehend
137 extreme dust events but more importantly to provide accurate information to decision
138 makers beforehand. Because of that, it has been checked if the results from dust models
139 (BSC-DREAM8b and NMMB/BSC-Dust) are in agreement with observations as the
140 relationship between certain meteorological patterns and extreme African dust events
141 can provide useful information for human health, air traffic controllers, or to predict
142 different climate change scenarios. However, dust models have proved to fail in certain
143 occasions under extreme dust events (Mamouri, Ansmann et al. 2016) mainly because
144 the scale used by models is not small enough to appreciate such phenomena.

145 The aim of this paper is to procure an overview of the available dust observations
146 obtained from remote sensing techniques at different locations in the IP, to derive the
147 aerosol optical property profiles from such observations and to compare them against
148 the results computed from models. The paper is organized as follows. The instruments
149 and methodology are briefly described in Sect. 2. Sect. 3 deals with the description of
150 the synoptic situation and columnar aerosol optical properties from sun and sky spectral
151 radiometers. In section 4, vertically-resolved optical properties are discussed. Section 5
152 presents the performance of the dust models. Finally, conclusions can be found in Sect.
153 6.

154 **2 Instruments and methodology**

155 2.1 AERONET CIMEL CE-318 Sun-photometers in the IP.



156 The Aerosol Robotic NETWORK (AERONET) is a global ground-based network of
157 sun/sky multi-wavelength CIMEL CE-318 sun-photometers that provides relatively
158 long-term records of atmospheric columnar aerosol optical properties (Holben, Eck et
159 al. 1998). The CIMEL spectral sun-photometer measures the direct solar irradiances
160 with a field of view of approximately 1.2° and the sky radiances (in the almucantar and
161 principal plane scenarios), at several spectral channels (see table 1). The direct-sun
162 measurements are used to obtain the spectral AOD, Ångström exponent at several
163 wavelength pairs and precipitable water vapor, approximately every 15 min. The
164 estimated AOD uncertainty (mainly due to the calibration) is between 0.01 and 0.02
165 (Holben, Eck et al. 1998).

166 The sky radiance measurements can be inverted to estimate aerosol optical properties
167 such as the size distribution, the percentage of spherical particles in the aerosol mixture,
168 several microphysical parameters describing the total, fine and coarse aerosol modes
169 and numerous spectral quantities: complex refractive index, single scattering albedo,
170 phase function, asymmetry parameter, extinction and absorption optical depths. The
171 aerosol properties retrieved are hence used for calculating the broad-band fluxes at
172 the bottom and top of the atmosphere, the radiative forcing and forcing efficiencies are
173 also provided. A detailed description of the version 2 AERONET inversion products is
174 given by (Holben, Tanre et al. 2001). Table 1 shows the six AERONET stations
175 distributed in the IP that were considered in this study.

176



177 **Table 1 – Summary of the sites considered in the study, main characteristics of the**
 178 **AERONET sun-photometers and EARLINET lidars used, and lidar measurement**
 179 **time.**

Site	Long. (°)	Lat. (°)	Altitude (m a.s.l.)	AERONET Sun photometer channels for AOD (nm)	EARLINET Lidar channels (nm)			Lidar measurement time	
					Elastic	Raman	Vertical resol. (m)	Start time	Stop time
Barcelona	2.11° E	41.39° N	115	440, 675, 870, 1020	355, 532 total, 532 cross, 1064	387, 407, 607	3.75	08:11 UTC (23 Feb)	23:54 UTC (23 Feb)
Burjassot	0.42° W	39.51° N	60	340, 380, 440, 500, 675, 870, 1020, 1640	355 cross and parallel	387	15	-	-
Cabo da Roca	9.50° W	38.78° N	140	340, 380, 440, 500, 675, 870, 1020	-	-	-	-	-
Évora	7.91° W	38.57° N	293	340, 380, 440, 500, 675, 870, 1020	355, 532, 532 cross, 1064	387, 607	30	00:00 UTC (20 Feb)	23:59 UTC (23 Feb)
Granada	3.61° W	37.16° N	680	340, 380, 440, 500, 675, 870, 1020	355, 532 parallel, 532 cross, 1064	387, 407, 607	7.5	12:00h UTC (20 Feb)	18:00h UTC (20 Feb)
								19:00h UTC (20 Feb)	21:00h UTC (20 Feb)
								07:31h UTC (21 Feb)	14:21h UTC (21 Feb)
								07:31h UTC (22 Feb)	20:00h UTC (22 Feb)
Madrid	3.72° W	40.45° N	669	340, 380, 440, 500, 675, 870, 1020	355, 532, 1064	387, 407, 607	7.5 (elastic), 3.75 (Raman)	21:00h UTC (22 Feb)	23:36h UTC (22 Feb)
								05:00h UTC (23 Feb)	08:00h UTC (23 Feb)
								11:00h UTC (23 Feb)	11:52h UTC (23 Feb)

180

181 2.2 EARLINET lidars in the IP

182

183 The European Aerosol Research Lidar Network, EARLINET, aims at creating a
 184 quantitative, comprehensive, and statistically significant database for the horizontal,
 185 vertical, and temporal distribution of aerosols on a continental scale, providing the most
 186 extensive collection of ground-based data for the aerosol vertical distribution over
 187 Europe (Pappalardo, Amodeo et al. 2014). In this work four Iberian EARLINET



188 stations (Barcelona, Madrid, Évora and Granada) provided lidar data, all of them
189 equipped with multi-wavelength lidars and some of them with depolarization
190 capabilities (see Table 1). Burjassot lidar station was not available at this moment.

191 On a regular basis, the EARLINET protocol establishes that lidar measurements have to
192 be carried out on Monday (at 14 UTC and at sunset) and on Thursday (sunset).
193 However, under exceptional events, as the one described in this work, these stations
194 perform additional measurements in order to register the phenomena as long as possible.
195 Then, lidar signals were averaged over 30 minute periods in order to guarantee a proper
196 signal-to-noise ratio throughout the vertical column. The criteria followed to choose
197 such periods is based on the representation of the dust plume but also on the data
198 availability at atmospheric levels where Rayleigh computation can be accomplished
199 since the aerosol burden during this event was certainly high and produced a great
200 radiation extinction, which hampered the Rayleigh retrieval. In this work, lidar
201 measurements at each station were performed at the periods specified in Table 1.

202 Vertically resolved particle coefficients were derived by means of the Klett-Fernald
203 algorithm (Klett 1981, Fernald 1984). This algorithm requires an assumption of the lidar
204 ratio (LR), defined as the particle extinction (α) to particle backscatter (β) coefficients
205 ratio, and for mineral dust we have considered a value of 50 sr (Guerrero-Rascado, Ruiz
206 et al. 2008, Guerrero-Rascado, Olmo et al. 2009, Muller, Heinold et al. 2009, Muller,
207 Ansmann et al. 2010, Preissler, Wagner et al. 2011). If possible, α and β coefficient
208 profiles were retrieved independently (Ansmann, Wandinger et al. 1992), which in turn
209 allow computing the vertically-resolved LR. Given the fact that the LR is an intensive
210 parameter, it provides useful information for the analysis of aerosol optical properties.
211 Another intensive variable is the Ångström exponent (Ångström 1964). It is inversely
212 related to the size of particles: the greater the exponent is, the smaller the particles are



213 and vice versa (Amiridis, Balis et al. 2009). This is defined for the wavelength pair (λ_1
214 and λ_2) as:

$$215 \quad \mathring{a}_\alpha = -\frac{\log[\alpha(\lambda_1)/\alpha(\lambda_2)]}{\log[\lambda_1/\lambda_2]} \quad (1)$$

216 However, extinction coefficients were not always available but the three backscatter
217 coefficients. Because of that, the backscatter-related Ångström exponent is also
218 estimated, and the relationship to the aerosol size is similar than the previous definition,
219 although it is affected by other parameters such as refractive index so the relationship
220 should not be straightforward. Last but not least, lidar systems equipped with
221 depolarization channels procure relevant information about the aerosol type because
222 backscatter signals related to the cross and parallel-polarized component varies
223 depending on aerosol shape.

224 With regard to the errors associated to the measurements, we made use of the Monte-
225 Carlo technique so as to estimate the uncertainties of the vertically-resolved backscatter
226 and extinction coefficients. This technique is based on the random extraction of new
227 lidar signals, each bin of which is considered a sample element of a given probability
228 distribution with the experimentally observed mean value and standard deviation. The
229 extracted lidar signals are then processed with the same algorithm to obtain a set of
230 solutions from which the standard deviation is inferred as a function of height
231 (Pappalardo, Amodeo et al. 2004).

232 2.3 Description of the models evaluated and methodology

233 The present analysis utilizes the operational 72-hour dust forecasts of the BSC-
234 DREAM8b (Perez, Nickovic et al. 2006, Basart, Perez et al. 2012) and the
235 NMMB/BSC-Dust (Perez, Haustein et al. 2011) models



236 (<http://www.bsc.es/ess/information/bsc-dust-daily-forecast>) for the period from 19 to 22
 237 February 2017. Both models are developed and operated at the Barcelona
 238 Supercomputing Center (BSC). Table 2 summarizes the main parameters used in the
 239 configuration of the models.

240 **Table 2. Main parameters of the dust models used in this study.**

241

	BSC-DREAM8b	NMMB/BSC-Dust
Meteorological driver	Eta/NCEP	NMMB/NCEP
Model domain	North Africa-Middle East-Europe (25° W – 60° E and 0° – 65° N)	
Initial and boundary conditions	NCEP/GFS data (at 0.5° × 0.5° horizontal resolution) at 12 UT are used as initial conditions and boundary conditions at intervals of 6 hours	
Horizontal resolution	0.33° x 0.33°	
Vertical resolution	24 Eta-layers	40 σ -hybrid layers
Time step	1h	3h
Dust size bins	8 (0.1–10 μm)	
Radiation interactions	Yes	Yes
Dust initial condition	24 h forecast from the previous day's model run	

242

243 The modeled dust extinction values at 550 nm are directly compared with the observed
 244 particle extinction values at 532 nm because of the wavelength proximity and the low
 245 spectral extinction dependence of mineral dust (see Section 4). In order to have
 246 continuous observations and to maximize their number, day and nighttime inversions of
 247 particle backscatter coefficients are used and converted to extinction by multiplying
 248 them by a constant lidar ratio of 50 sr. The vertical resolution of both dust models is
 249 much coarser than the lidar vertical resolution. In order to evaluate the models'



250 capability to reproduce the vertical distribution of the dust extinction coefficient, the
251 original lidar vertical resolution is downgraded to the resolution of the modeled profiles.
252 For the horizontal resolution, the lidar data can be considered as point observations,
253 while the models represent uniform pixels of 0.33° resolution (~ 33 km). The temporal
254 resolution is also different: while the models provide instantaneous profiles with time
255 steps of 1 hour for BSC-DREAM8b and of 3 hours for NMMB/BSC-Dust, the lidar
256 profiles are averaged over 30 min. Here we have compared each modeled profile at
257 time t with a 30-min. averaged lidar-derived profile included in the interval $[t, t+1$
258 hour]. The forecast skill analysis is performed in terms of two vertically integrated
259 statistical indicators, namely the fractional bias (FB), and the correlation coefficient (r
260), as well as in terms of the center of mass (CoM). The fractional bias is a normalized
261 measure of the mean bias and indicates only systematic errors, which lead to an
262 under/overestimation of the estimated values. The linear correlation coefficient is a
263 measure of the models' capability to reproduce the shape of the aerosol profile. The
264 vertical integration is made from the lowest pair of simultaneously available model and
265 observed values up to 6 km. No lower limit was fixed because of the dust plume
266 proximity to the ground surface. The upper limit was fixed to 6 km because nearly no
267 dust was detected above that height. The CoM was approximated by the particle
268 backscatter weighted altitude as defined in (Mona, Amodeo et al. 2006) who noted that
269 this approximation “exactly coincides with the true center of mass if both composition
270 and size distribution of the particles are constant with the altitude”.

271 In the following sections we evaluate the model performances for forecasts of 24 hours
272 (Section 5.1) and then we compare these forecasts to longer ones of 48 and 72 h
273 (Section 5.2) to see how the forecast skill behaves as the lead time increases. A forecast
274 (or a lead time) of 24 h represents all forecasts in the range $[0; 23h]$ since the model

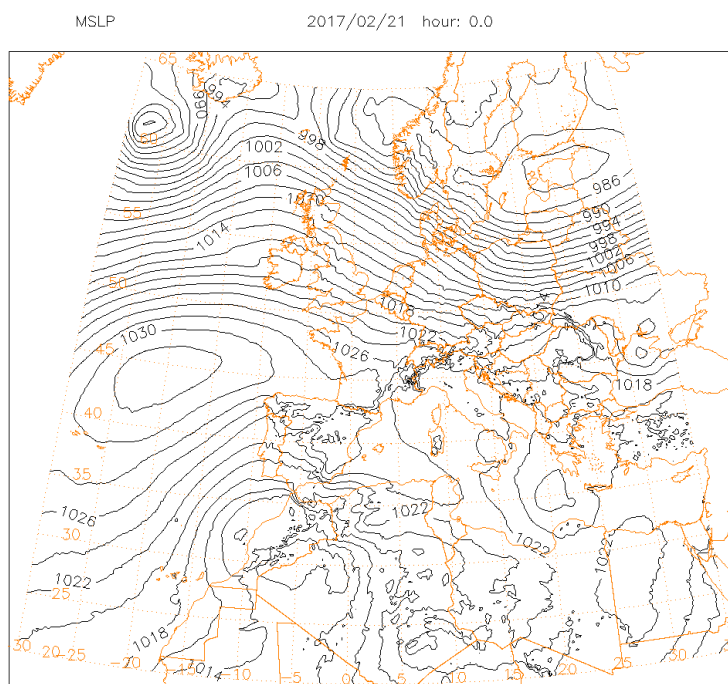


275 initialization. 48 and 72 h forecasts represent all forecasts in the range [24; 47h] and
276 [48; 71h] since the model initialization, respectively.

277 **3 Synoptic situation and columnar properties**

278 3.1 Synoptic situation

279 During the period from 20 to 23 February 2017, the synoptic situation in the IP was
280 dominated by the influence of an anticyclone centered northwest from the Western
281 coast, extending in ridge to South Central Europe, as illustrated in the analysis of the
282 mean sea level pressure at 00 UTC on 21 February (Fig.1). During this period, the low
283 tropospheric flow over the IP was characterized by moderate easterly and southeasterly
284 winds, reinforced by the existence of a low centered over Morocco. The streamlines at
285 850 hPa (not shown) indicate the persistence of an atmospheric flow advecting air from
286 the central North Africa (Algeria, Tunisia) crossing the IP. On 23 February the
287 intensification and northward shift of the Moroccan low, broke up the anticyclonic flow
288 over the South of Iberia, originating weak precipitation events in several locations in the
289 south of Portugal and Spain. The synoptic conditions changed sharply on 24 February
290 with the passage of a frontal system that affected all the IP.



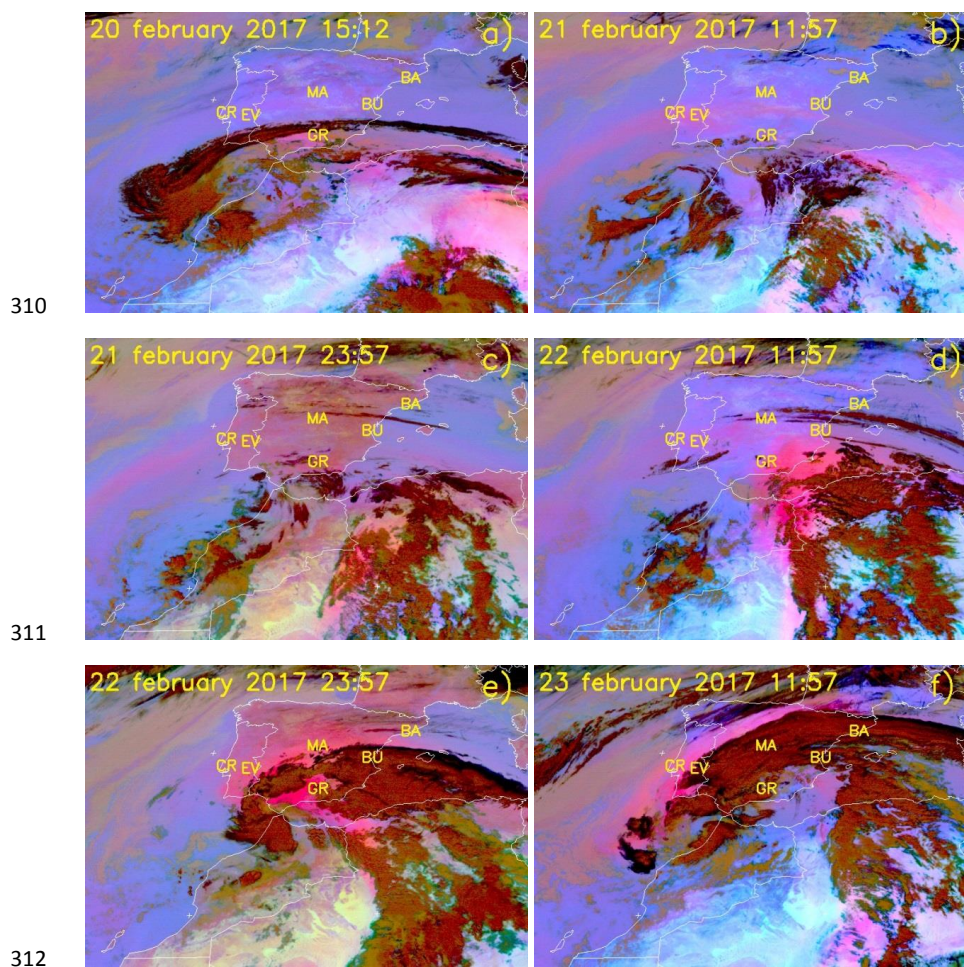
291
292 **Fig. 1. European Centre for Medium-Range Weather Forecasts (ECMWF)**
293 **analysis of the Mean sea level pressure at 21/02/2017 00:00 UTC.**

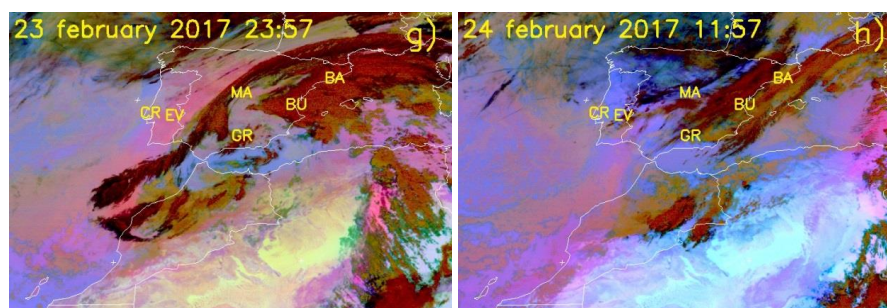
294 Fig. 2 presents RGB composites based upon the combination of infrared channels (8.7,
295 10.8 and 12.0 μm) from the Spinning Enhanced Visible and InfraRed Imager (SEVIRI)
296 on board Meteosat-10, showing the dust transport evolution (magenta) from 20 to 24
297 February 2017. The dust was transported across the Alboran Sea (western
298 Mediterranean Sea) and infiltrated in southern Iberian atmosphere on 20 February
299 (Fig.2a), gradually transported towards west and north by the easterly and southeasterly
300 winds (Figs.2b and 2c), affecting the southern and western sites (CR, EV, GR). On the
301 22 February the dust intrusion was reinforced by a thick plume that progressively
302 entered the IP through the southeastern coast (Fig. 2d) extending north and westwards
303 and affecting all sites represented in the images (Fig. 2e). This new intrusion was
304 accompanied by the presence of high clouds that on the 23 February affected most of



305 the IP, associated with the intensification and northward shift of the Moroccan low
306 (Figs.2f and 2g). The arrival of a frontal system from northwest on the 24 February
307 interrupted the North African dust flow, pushing it towards the central Mediterranean
308 regions (Fig. 2h).

309





313

314 **Fig. 2. Meteosat RGB composites showing the evolution of the dust plume from 20**
315 **to 24 February 2017. The Iberian sites considered in the study are also represented**
316 **in the images: Barcelona (BA), Burjassot (BU), Cabo da Roca (CR), Évora (EV),**
317 **Granada (GR) and Madrid (MA).**

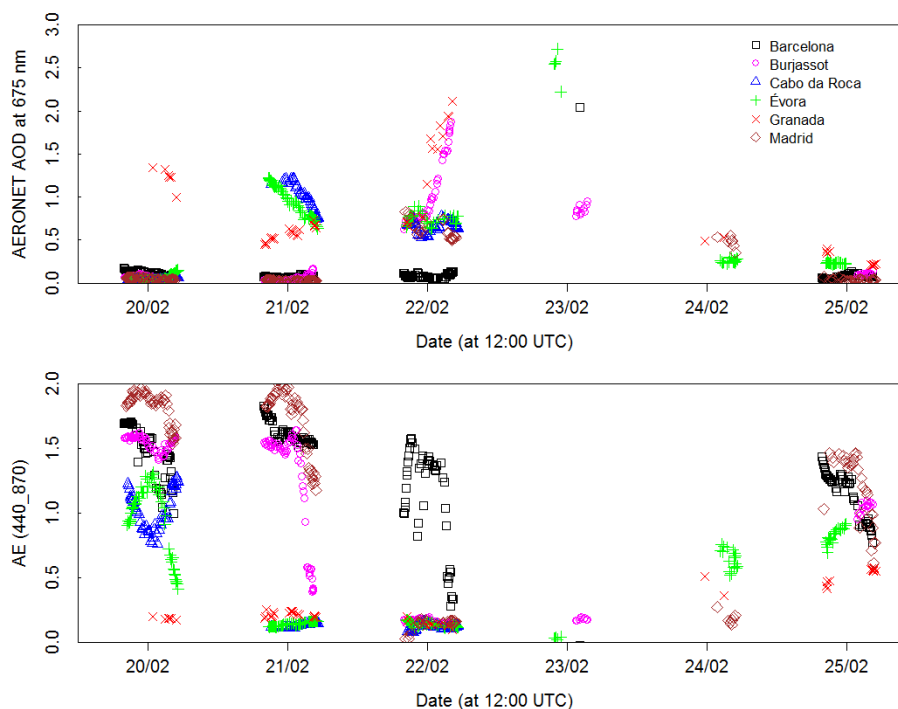
318

319 3.2 Columnar properties

320 The desert dust plume entered the IP from the South on the 20 February, and then it
321 gradually reached the northwest and later on the eastern part of the IP. Fig. 3 shows the
322 time series data of AOD at 675 nm and Ångström exponent (440 and 870 nm), from 20
323 to 25 February 2017 in six sites distributed across the IP. An increase of the AOD was
324 first noticed in Granada site on the 20 February, where the AOD values reach about 1.5,
325 accompanied by very low values of AE, typical of desert dust intrusions, which is
326 confirmed by the Meteosat composite in Fig. 2a. The dust plume maintains its influence
327 over Granada and extends towards the western part of IP, affecting in the next day also
328 Évora and Cabo da Roca sites, with AOD values ranging between about 0.6 and 1.2,
329 once again with very low AE (<0.2). The dust transport continues and on the 22
330 February, during daytime, desert dust is detected in all stations except for Barcelona
331 where it is measured in the next day. Still on the 22 February, extremely high AOD
332 values are reached in Granada and Burjassot (> 2.0) and moderately high in Madrid,
333 Évora and Cabo da Roca ($0.5 < \text{AOD} < 1.0$), with AE values lower than 0.2 for all these



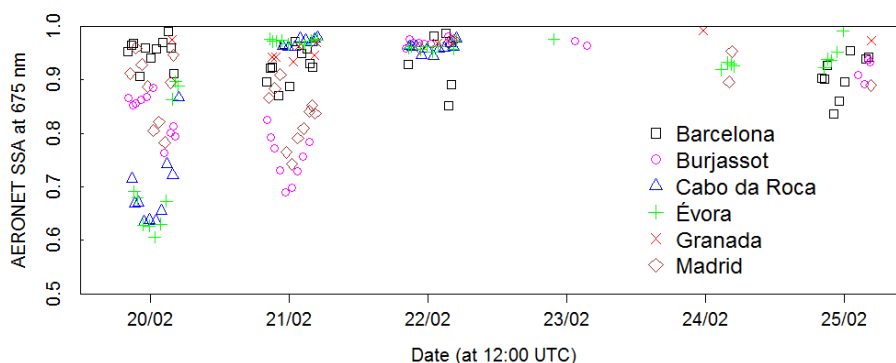
334 stations. On the 23 February there are only a few AERONET measurements available
335 due to the persistence of clouds over the region, nevertheless the AOD is still
336 considerably high (>2.0) for Évora and Barcelona, with corresponding AE values
337 around zero in these sites. As mentioned before, the frontal system on the 24 February
338 interrupted the dust transport and the AOD values on the 24 and 25 February show a
339 consistent decrease with a corresponding increase of the AE.



340
341

342 **Fig. 3. – AERONET AOD at 675 nm and AE (440 and 870 nm) from 20 to 25**
343 **February 2017 in six sites distributed across the IP.**

344



345

346 **Fig. 4 - AERONET SSA at 675 nm from 20 to 25 February 2017 during the event**
347 **for six sites distributed across the IP.**

348 The single scattering albedo is characterized by relatively high values in all the stations
349 during the dust event, showing the predominant dispersive nature of these particles. The
350 lower SSA values in the first two days (greater absorption) in some of the sites (BU,
351 CR, EV, MA) depicted in Fig.4, are related with polluted air masses coming from
352 northwestern Europe (not shown here).

353 4. Vertically-resolved optical properties

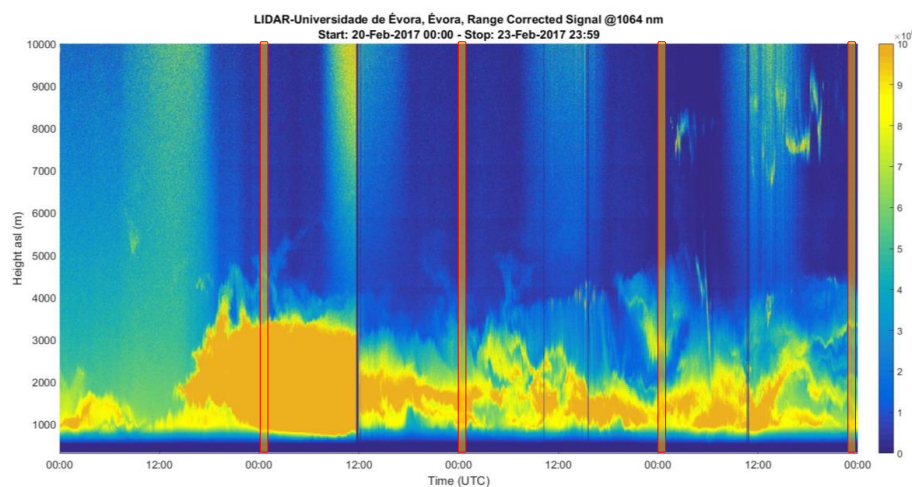
354

355 ÉVORA

356 Fig. 5 represents the RCS during 4 days, 24 hours per day, which provides a very
357 detailed overview of the phenomenon. It can be seen that the African dust outbreak was
358 especially intense at the beginning of the event, from 20 (12:00 UTC) to 21 (12:00
359 UTC) February. Four different periods have been selected so as to analyze aerosol
360 optical properties from the African plume observed in Évora (highlighted again in red in
361 Fig. 5). Nighttime measurements have been chosen for the analysis in order to estimate
362 accurately such properties given the fact that independent extinction from Raman
363 signals was available at this lidar station. The first period (21st Feb from 0:00-0:30



364 UTC), presents the highest backscatter coefficient values out of all periods evaluated, so
365 a especial attention will be paid to this period (Fig. 6). Notwithstanding the other 3
366 periods are also analyzed and they can be seen in the supplementary material Fig. S1,
367 S2 and S3. Mean aerosol optical properties are exposed in this latter Table (3) for
368 specific atmospheric layers where in principle the dust plume is representative. For
369 instance, the first period analyzed presents an African dust plume that reaches also 5 km
370 height asl, however maximum values of particle backscatter coefficient are reached at
371 3222 m asl and from 4 to 5 km asl the presence of African dust is very small according
372 to particle backscatter coefficient profiles. For this reason, it is considered more
373 appropriate to evaluate the atmospheric layer detected between 1.5-3.5 km asl. At this
374 atmospheric layer, backscatter-related Ångström exponent at the wavelength pairs:
375 532/355, 1064/532 and 1064/355 were found to be 0.08 ± 0.33 , 0.62 ± 0.04 and 0.42 ± 0.13
376 respectively and the extinction-related Ångström exponent at 532/355 nm was estimated
377 to be 0.16 ± 0.45 . These small values are typical for dust as previously reported during
378 extreme African dust outbreaks (Mamouri, Ansmann et al. 2016) (Guerrero-Rascado,
379 Olmo et al. 2009, Preissler, Wagner et al. 2011). The other periods also show relatively
380 low backscatter-related Ångström exponents and Ångström exponent values, which in
381 principle indicates a large particle size.



382

383 **Fig. 5. RCS at 1064 nm on 20-23 February 2017 for the period established between**
384 **0:00h-23:59 UTC respectively (Évora, 293 m asl).**

385 Since Raman signals were available and extinction coefficients were obtained
386 independently, particle lidar ratios were derived as well. The dust layer located between
387 1.5-3.5 km asl on 21Feb (00:00 UTC) presented a lidar ratio of 40 ± 8 sr and 61 ± 18 sr at
388 355 and 532 nm, respectively. Our estimates at 355 nm are in agreement with Mona et
389 al. that found a mean lidar ratio at 355 nm of 38 ± 15 sr for three years of Raman lidar
390 measurements of Saharan dust (Mona, Amodeo et al. 2006). On the other hand, lidar
391 ratio at 532 nm is found greater than the lidar ratio at 355 nm for the first period
392 analyzed (21 Feb, 00:00 UTC), which is not usual for dust particles as it has been
393 already pointed out by other authors (Muller, Ansmann et al. 2010). Nevertheless, this
394 trend is only observed in the first period analyzed, the other three analyzed periods
395 show a lidar ratio at 532 lower than the lidar ratio at 355 nm. The reason behind this
396 observation (high unexpected lidar ratio values at 532 nm) can be attributed to non-
397 accurate retrievals handicapped by the high aerosol load, which produces great
398 extinction and consequently a scarce lidar signal to be evaluated. It is noteworthy to



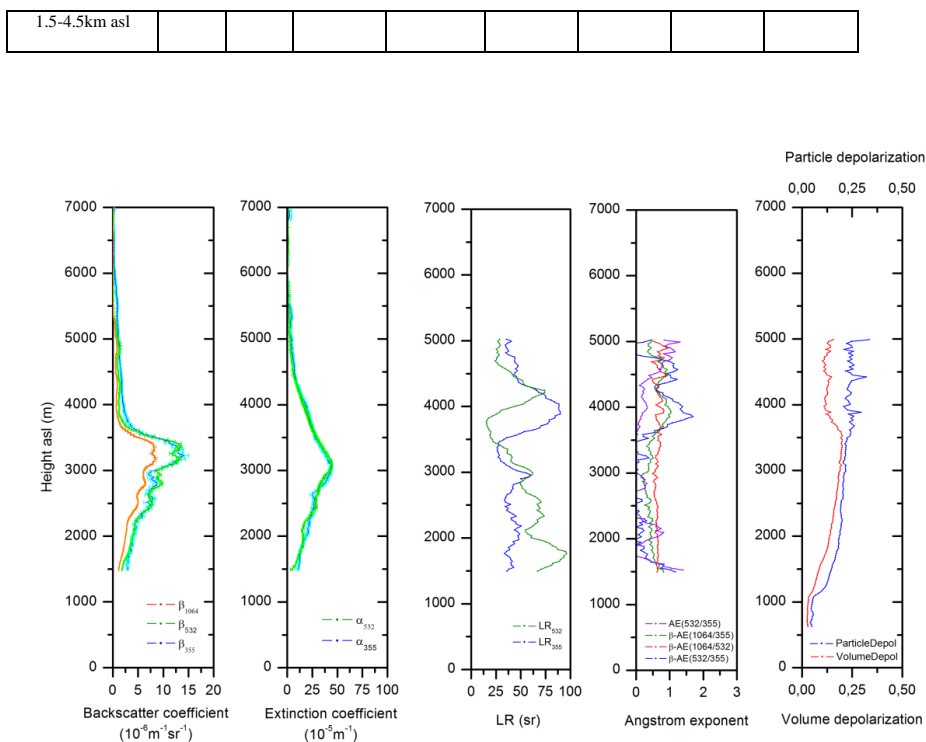
399 mention that the standard deviation of the mean lidar ratio at 532 nm on 21Feb (00:00
 400 UTC) is significantly higher compared to the rest of studied period. On another note,
 401 lidar ratio at 355 nm on 23 Feb (at 00:00 and 23:39 UTC) seems a bit higher than values
 402 reported in literature (Mona, Amodeo et al. 2006) and it could be due to a decrease of
 403 the African dust outbreak intensity and therefore a greater proportion of local aerosol
 404 might be present in the atmosphere. Lidar ratio at 532 nm in all cases (apart from the
 405 first period) are consistent with literature since typical values range 35-45 sr for typical
 406 desert dust (Mamouri, Ansmann et al. 2013, Nisantzi, Mamouri et al. 2015, Mamouri,
 407 Ansmann et al. 2016). In addition, particle and volume depolarization ratio were
 408 0.19 ± 0.02 and 0.16 ± 0.03 for the aforementioned atmospheric layer on 21Feb 00:00
 409 UTC. These two latter parameters are constant with altitude, which indicates that no
 410 changes in the aerosol type is observed within the atmospheric layer of interest. They
 411 are also very similar for the four periods studied, however the last period of study
 412 indicates lower particle and volume depolarization values that is associated with the
 413 decrease of intensity of the Saharan dust outbreak and a greater contribution of local
 414 aerosols.

415 **Table 3. Summary of mean aerosol optical properties retrieved for the 4 periods**
 416 **analyzed from Raman lidar measurements (Évora).**

Atmospheric layer	LR ₃₅₅ (sr)	LR ₅₃₂ (sr)	β-AE 1064-532	β-AE 532-355	β-AE 1064-355	AE 532-355	δ-vol.	δ-part.
00:00 UTC-21Feb 1.5-3.5km asl	40±8	61±18	0.62±0.04	0.08±0.33	0.42±0.13	0.16±0.45	0.16±0.03	0.19±0.02
00:00 UTC-22Feb 1.5-4km asl	45±4	38±8	0.76±0.12	-0.12±0.23	0.44±0.08	0.16±0.19	0.16±0.01	0.21±0.01
00:00 UTC-23Feb 1.5-5km asl	52±7	40±9	1.28±0.33	-0.62±0.48	0.58±0.19	0.01±0.27	0.16±0.02	0.19±0.01
23:39 UTC-23Feb	55±12	34±8	1.00±0.18	-0.96±0.29	0.28±0.17	0.18±0.24	0.12±0.01	0.15±0.01



417



418

419 **Fig. 6. Backscatter coefficient, extinction coefficient, lidar ratio, Ångström**
420 **exponents, and particle and volume depolarization profiles at 00:00 UTC on 21,**
421 **February 2017 at Évora.**

422 **GRANADA**

423 In Granada, four lidar measurements were carried out during the extreme African dust
424 outbreak. In particular for the periods: 12:00-18:00 and 19:00-21:00 UTC on 20
425 February, 07:31-14:21 UTC on 21 February, and 07:31-20:00 UTC on 22 February.
426 Such measurements are represented in Fig. 7. The red highlights indicate as previously
427 the selected periods where vertically-resolved aerosol optical properties have been
428 derived. Such vertical profiles can be seen in the supplementary material in Fig. S4, S5,
429 S6 and S7. For a better comprehension of these data, mean aerosol optical properties are



430 presented in table 4 for the periods highlighted in red and for the atmospheric layer
431 where the dust plume is registered. In general terms, the maximum altitude of the dust
432 plume was registered at 4 km asl approximately and it was maintained relatively
433 constant throughout the four lidar measurements. For certain periods (13:30-14:21 UTC
434 on 21st Feb) intensification of the RCS is observed at the top of the dust plume, which
435 may indicate cloud formation processes related to mineral dust.

436 Concerning intensive aerosol optical properties, backscatter-related and extinction-
437 related Ångström exponents were found certainly low, in accordance with previous lidar
438 observations, which indicate a large aerosol size. The Raman retrieval could be
439 performed only for the period 19:00-21:00 UTC on 20 February since it was not
440 possible to perform during nighttime on other days. On 22 February, the African dust
441 outbreak was so intense that produced large extinction and hampered proper retrieval.
442 So, lidar ratios obtained at Granada were 52 ± 7 and 53 ± 6 at 355 and 532 nm
443 respectively. With regard to particle and volume depolarization ratios, these parameters
444 show similar and consistent values to data obtained in previously cited lidar station.
445 Nevertheless, it is noteworthy to mention that the last analyzed period (12:30 UTC on
446 22Feb) exhibits the greatest particle and volume depolarization ratios observed in all
447 lidar stations. These high values point out that a large backscatter signal related to the
448 cross-polarized component is registered, which in turn is produced by non-spherical
449 particles. This is associated to an enlargement on the contribution of mineral dust due to
450 the reinforcement of the dust plume coming from Africa. Such reinforcement of the dust
451 plume was observed on 22 Feb according to the synoptic meteorological situation (see
452 section 3). In fact, it was not possible to retrieve proper lidar products for measurements
453 carried out on 22 Feb from 17:30 UTC on, given the large extinction of radiation
454 produced by the high contribution of mineral dust.

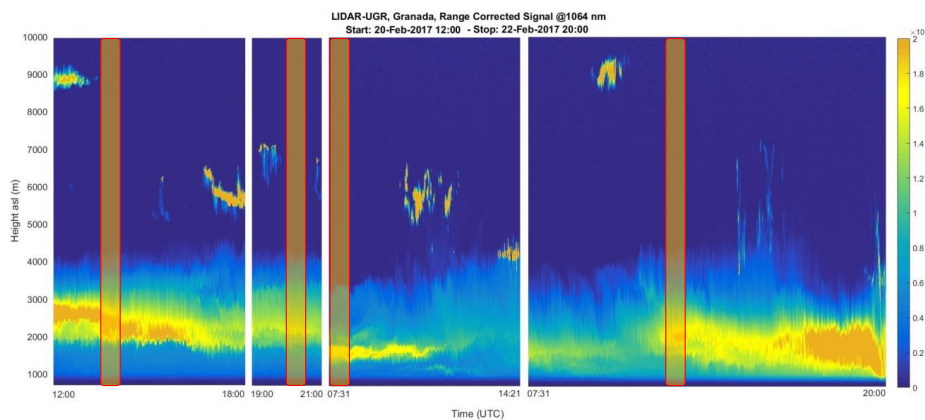


455 **Table 4. Summary of mean aerosol optical properties retrieved for the 4 periods**
 456 **analyzed from Raman lidar measurements (Granada).**

Atmospheric layer	LR ₃₅₅ (sr)	LR ₅₃₂ (sr)	β -AE 1064-532	β -AE 532-355	β -AE 1064-355	AE 532-355	δ -vol.	δ -part.
13:30 UTC-20Feb 2.0-4.0 km asl			0.27±0.12	0.19±0.30	0.24±0.04		0.19±0.03	0.22±0.04
20:00 UTC-20Feb 1.8-4.0 km asl	52±7	53±6	0.19±0.08	0.54±0.21	0.32±0.07	0.51±0.43	0.20±0.02	0.25±0.03
07:31 UTC-21Feb 1.5-3.4km asl			0.86±0.07	0.64±0.13	0.77±0.08		0.18±0.03	0.28±0.01
12:30 UTC-22Feb 1.5-4.0 km asl			0.39±0.12	0.32±0.17	0.36±0.07		0.26±0.01	0.31±0.02

457

458



459

460 **Fig. 7. RCS at 1064 nm on 20 February (12:00-18:00, 19:00-21:00 UTC), 21**
 461 **February (07:31-14:21 UTC), 22 February (07:31-20:00 UTC) 2017 at Granada**
 462 **(680 m asl).**

463

464

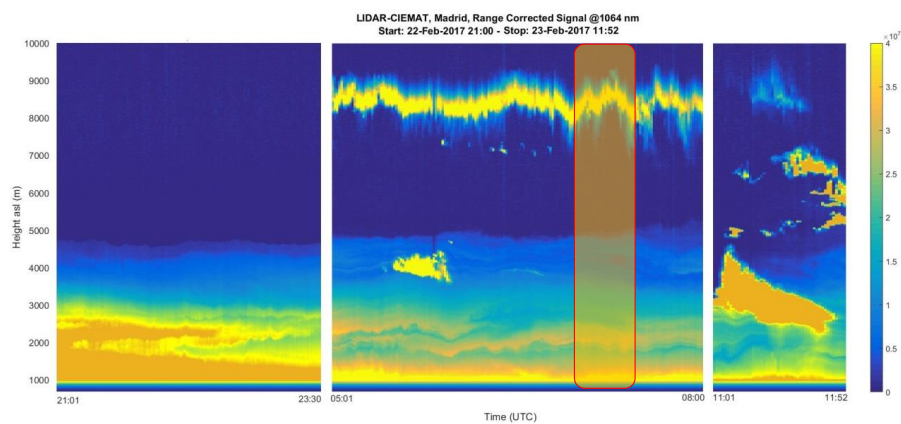
465 **MADRID**

466 In Madrid, as it occurred in Barcelona, the African dust plume was only detected in the
467 last stage of the African event when the reinforcement of the dust intrusion was
468 produced by synoptic flows (from 22 February on). Lidar measurements on 20 February
469 (not shown) at Madrid still did not present any sign of this extraordinary plume. During
470 this African event, three lidar measurements were available at this station: on 22 Feb
471 (21:00-23:36 UTC) and 23 Feb (05:00-08:00 and 11:00-11:52 UTC). They are
472 represented in Fig. 8. As it can be seen the thickness of the plume ranged from the
473 ground to 5 km asl and in the last lidar measurement the plume was accompanied by
474 thick clouds. Concerning the retrieval of vertically-resolved aerosol optical properties,
475 only the period 05:00-08:00 UTC (23 Feb) was considered for this purpose. Such
476 profiles are represented in Fig. 9, which concerns the period 06:59-07:29 UTC
477 highlighted in Fig. 8. Only one profile is presented given the fact that the extinction
478 observed on the first and third lidar measurement was again excessive at low
479 atmospheric levels due to the dust plume, so Rayleigh extinction could not be
480 appropriately computed. This is a problem we want to highlight as it appeared in several
481 lidar stations when addressing this study and performing the retrievals under such
482 extreme conditions (high aerosol load).

483 Finally, Fig. 9 presents 3 backscatter coefficient profiles at 1064, 532 and 355 nm and
484 their respective backscatter-related Ångström exponents. No particle extinction
485 coefficients could be obtained independently as Raman signal were too noisy due to the
486 aforementioned reasons. Maximum values of particle backscatter coefficient are reached
487 at 2200-2300 m asl. At this altitude β_{355} is $(6.85 \pm 0.09) \cdot 10^{-6}$, β_{532} is $(6.35 \pm 0.13) \cdot 10^{-6}$ and
488 β_{1064} is $(5.75 \pm 0.01) \cdot 10^{-6} \text{ m}^{-1} \text{ sr}^{-1}$. Mean backscatter-related Ångström exponents were
489 found to be 0.52 ± 0.34 , 0.28 ± 0.17 , 0.37 ± 0.22 at the wavelength pairs: 532/355,



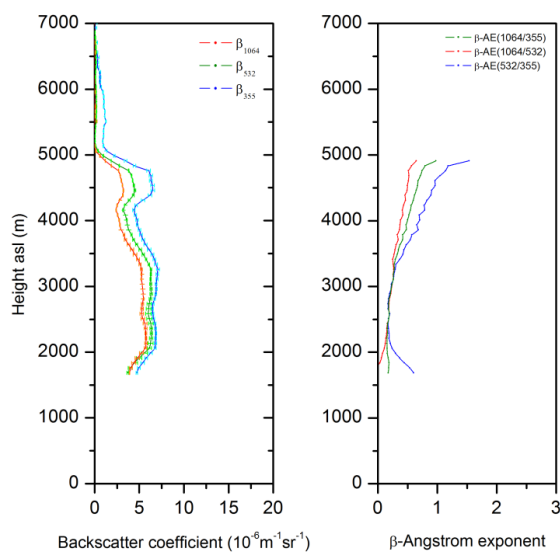
490 1064/532 and 1064/355 nm for the atmospheric layer established from lidar full overlap
491 height to 4900 m. These low backscatter-related Ångström exponents are in accordance
492 with previous lidar observations, which partially indicate a large aerosol size.



493

494 **Fig. 8.** RCS at 1064 nm on 22 February (21:00-23:36), 23 February (05:01-08:00
495 UTC), 23 February (11:00-11:52 UTC) 2017 at Madrid (669 m asl)

496



497

498 **Fig. 9. Backscatter coefficient and β -Ångström exponent profiles at 06:59 UTC on**
499 **23 February 2017 at Madrid.**

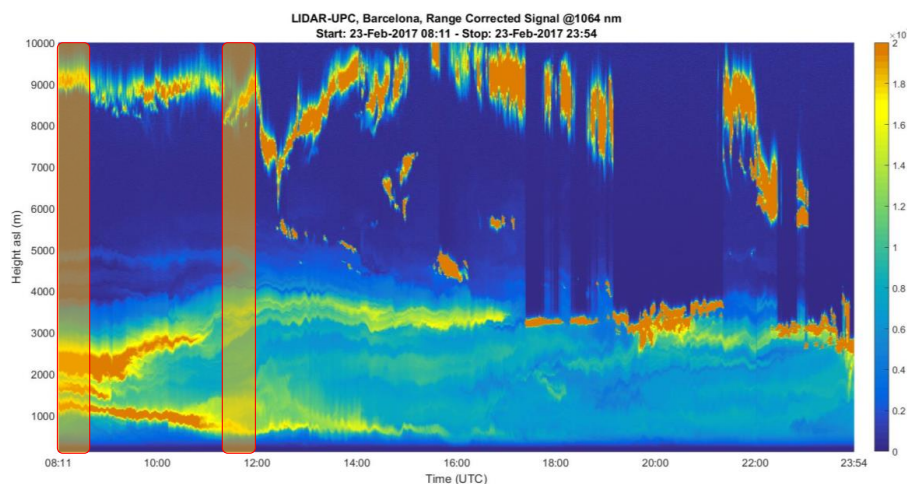
500 **BARCELONA**

501

502 According to the meteorological overview, Barcelona site was the latest place from the
503 time standpoint that was hit by the extraordinary African dust outbreak. As it can be
504 seen in Fig. 10 the African dust plume was registered throughout almost the entire 23
505 February. At the beginning of the lidar measurement (from 08:11 to 12:00 UTC), the
506 maximum altitude of the plume was detected at 5km asl approximately and after that it
507 decreased gradually until it reached the value of 3-3.5 km at 23:54 UTC. Two periods of
508 30 minutes have been considered more representative (at 08:11 and 11:34 UTC) to
509 retrieve aerosol optical properties from the lidar measurement. Both of them are
510 highlighted in red on Fig 10. As indicated in the color bar, the range corrected signal
511 (RCS) was considerably high for the atmospheric layer between 1 and 3 km during the



512 period 08:11-08:41 UTC. This is one of the reasons why this period of study was
513 selected since in principle this variable is a proxy of the intensity of the African dust
514 outbreak. The second period to be studied comprehends 11:34-12:04 UTC. In this case,
515 the dust plume is observed up to 5 km asl, although the structure is a bit different and
516 the RCS is lower than in the first period. It must also be noted that from 12:00 UTC on
517 the aerosol optical properties retrieval is quite complex since it is quite difficult to detect
518 a clean atmospheric layer so as to derive the Rayleigh extinction, which is mandatory to
519 infer the aforementioned aerosol optical properties. For the period 12:00-16:00 UTC
520 dispersed clouds can be observed at 5-7 km and from 17:00-18:00 UTC on clouds are
521 registered at the top of the dust plume layer (at 4 km), which prevents the Rayleigh
522 extinction computation. This latter observation is also interesting from the point of view
523 of cloud formation processes. Considering the evolution of the plume throughout the
524 entire lidar measurement at 4 km, it is plausible that African dust aerosol might act as
525 cloud nuclei (see RCS at 4 km from 18:00 to 23:54 UTC, the variable becomes more
526 intense than previously).



527

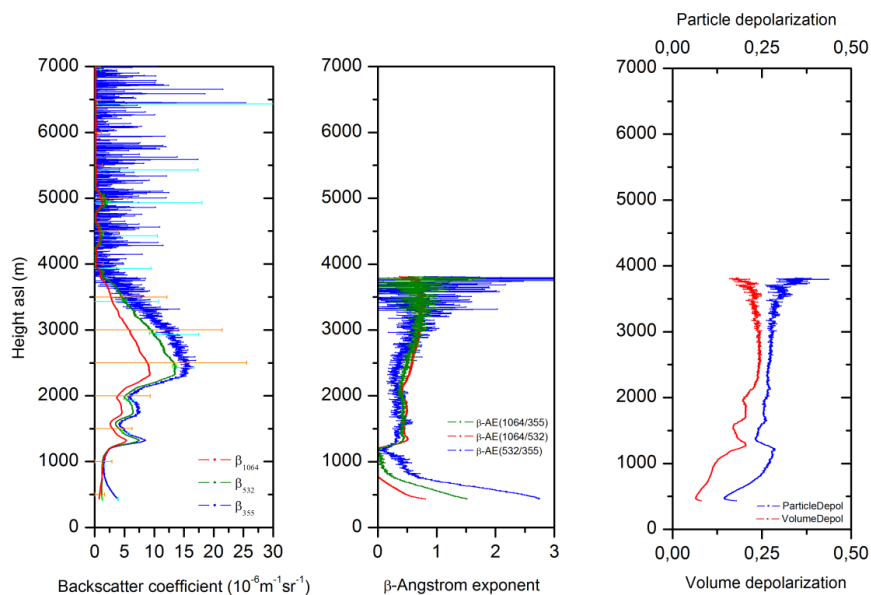


528 **Fig. 10. Range corrected signal (RCS) at 1064 nm on 23 February 2017 for the**
529 **period established between 08:11-23:54 UTC (Barcelona, 115 m asl).**

530 Fig. 11 shows aerosol optical properties obtained for the period 08:11-8:41 UTC. The
531 left panel represents the vertical profiles of particle backscatter coefficient at the three
532 wavelengths. The maximum values of this variable are reached at 2337 m asl. At this
533 altitude β_{355} is $(1.53 \pm 0.14) \cdot 10^{-5}$, β_{532} is $(1.35 \pm 0.04) \cdot 10^{-5}$ and β_{1064} is $(0.9 \pm 1.6) \cdot 10^{-5} \text{ m}^{-1}$
534 sr^{-1} . The mean backscatter-related Ångström exponents are 0.37 ± 0.14 , 0.45 ± 0.22 ,
535 0.42 ± 0.17 respectively at the wavelength pairs: 532/355, 1064/532, 1064/355 for the
536 altitude range 1-3km asl. In general terms, the greater the aerosol size the lower the
537 Ångström exponent. In this case the variable used is the backscatter-related Ångström
538 exponent, which is similar to the previous one, so the relation is affected by other
539 parameters such as refractive index, etc. other than the aerosol size. Nevertheless, these
540 values are typical for African dust (Guerrero-Rascado, Olmo et al. 2009), where aerosol
541 size plays an important role on this parameter. It is noteworthy to mention that the
542 vertical profile of the backscatter-related Ångström exponent is relatively constant
543 through the atmospheric layer detected between 1-3 km asl. With regard to volume and
544 particle depolarization ratio, we have found mean values of 0.21 ± 0.03 and 0.26 ± 0.01
545 respectively for the aforementioned atmospheric layer. In addition, a slightly increase of
546 depolarization ratio with altitude is observed. The reason behind it lies on the fact that
547 non-spherical particles tend to produce a higher backscatter signal related to the cross-
548 polarized component and higher depolarization ratios. African dust aerosols are well
549 known as non-spherical particles. So this observation would suggest that at higher
550 altitudes (from 1 to 3 km asl) the mineral dust is purer since depolarization ratios are
551 greater. In relation to Fig. 12 (11:34-12:04 UTC), the aerosol dust plume is a bit weaker
552 than in the previous period. The backscatter coefficient profiles are relatively lower and

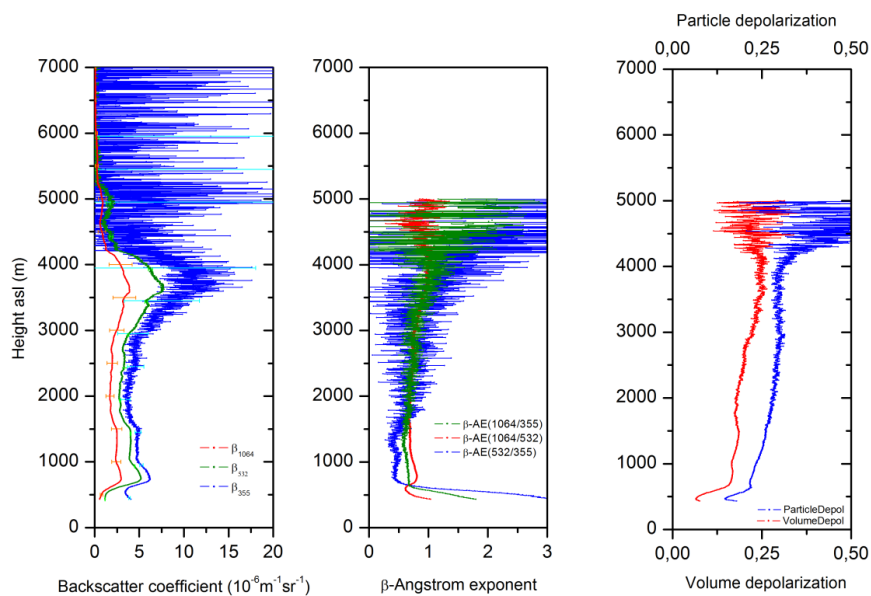


553 also the backscatter-related Ångström exponent profiles present higher values which
554 should indicate partially a smaller aerosol size. In this sense, the contribution of the
555 local aerosol may be greater. Considering these observations we can conclude that the
556 intensity of the African dust for this period is lower than the previous one. Volume and
557 particle depolarization ratios for the atmospheric layer situated at 1-3 km asl are similar
558 than in the previous period. The mean values are 0.19 ± 0.01 and 0.28 ± 0.02 respectively.



559

560 **Fig. 11. Backscatter coefficient, β -Ångström exponent, particle and volume**
561 **depolarization profiles at 08:11 UTC on 23 February 2017.**



562

563 **Fig. 12. Backscatter coefficient, β -Ångström exponent, particle and volume**

564 **depolarization profiles at 11:34 UTC on 23 February 2017.**

565



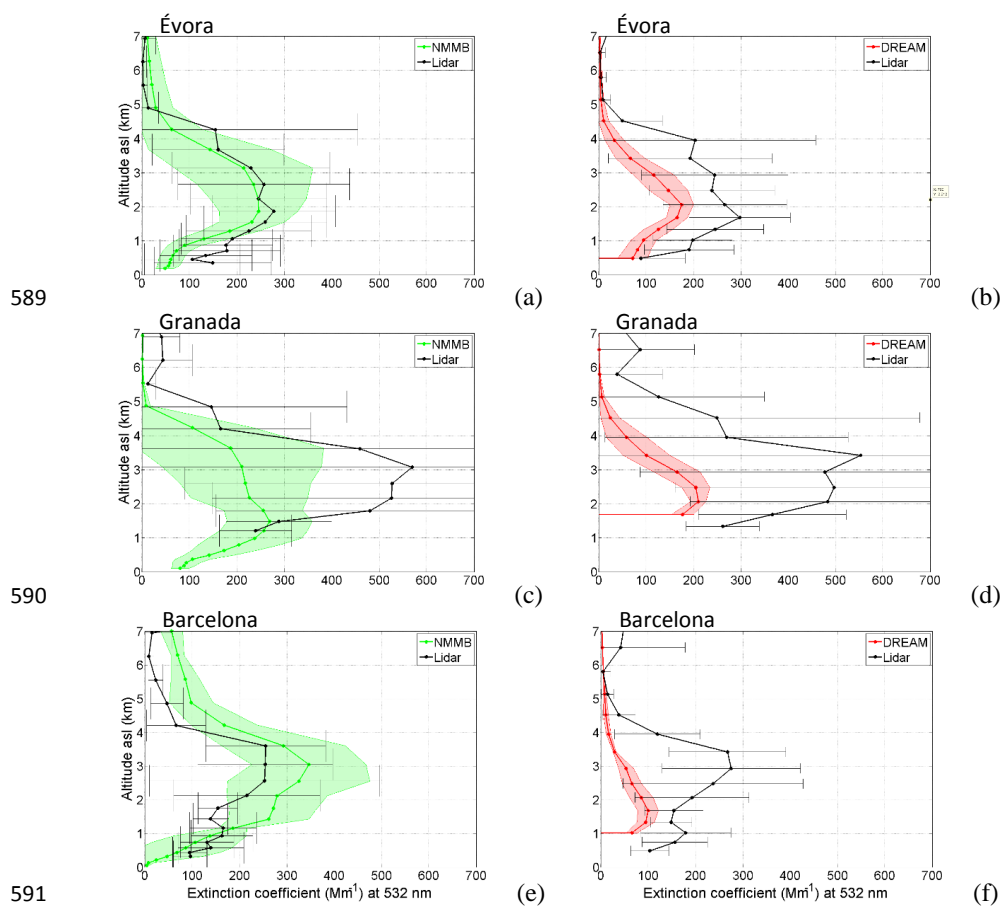
566 **5 Performance of dust models during intense events**

567

568 This section aims at examining the performance of dust models to predict the 3D
569 evolution of mineral dust during such intense outbreaks. The literature available on the
570 evaluation of modelled dust vertical profiles usually inspects the behavior of such
571 models on long time series or for a single moderate outbreak (Gobbi, Angelini et al.
572 2013, Santos, Costa et al. 2013, Mona, Papagiannopoulos et al. 2014, Biniotoglou,
573 Basart et al. 2015, Sicard, D'Amico et al. 2015), and only rarely for intense outbreaks
574 (Huneeus, Basart et al. 2016, Ansmann, Rittmeister et al. 2017, Tsekeri, Lopatin et al.
575 2017).

576 5.1 Forecast skill for a lead time of 24 h

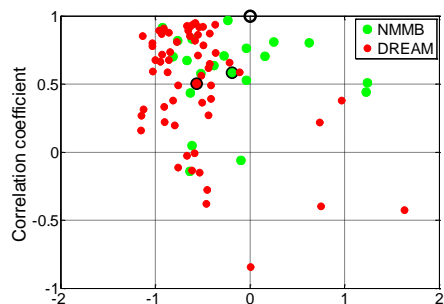
577 The results are presented for the three sites of Évora, Granada and Barcelona. There are
578 too few measured profiles in Madrid to allow for a statistical comparison. The
579 comparison of the temporal mean profiles of extinction coefficient is made for
580 NMMB/BSC-Dust and BSC-DREAM8b in Fig. 13. The temporal means are averaged
581 over the whole period (see caption of Fig. 13). For each individual profile the
582 correlation coefficient is plotted as a function of fractional bias in Fig. 14 and the
583 temporal evolution of the latter two parameters is shown in Fig. 15. In the latter figure
584 the time evolution of FB and r is also shown for lead times of 48 and 72 h and
585 discussed in Section 5.2. The mean values of the fractional bias, the correlation
586 coefficient and the center of mass for both models at each site are reported in Table 5.
587 Table 5 also contains these mean values for lead times of 48 and 72 h, which are
588 discussed in Section 5.2.



592 **Fig. 13.** Mean vertical distribution of mineral dust extinction coefficient estimated
593 by NMMB/BSC-Dust in (a) Évora, (c) Granada and (e) Barcelona and by BSC-
594 DREAM8b in (b) Évora, (d) Granada and (f) Barcelona. The period considered,
595 not always continuous, are 21 Feb. 12UT – 23 Feb. 23UT, 21 Feb. 12UT – 22 Feb.
596 19UT and 23 Feb. 08UT – 23 Feb. 21UT for Évora, Granada and Barcelona,
597 respectively. The model shaded areas and the error bars of the lidar represent the
598 standard deviations. All model forecasts are for a lead time of 24 h.

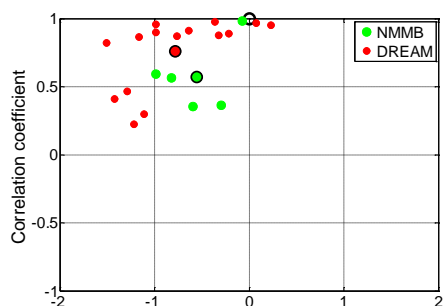


599



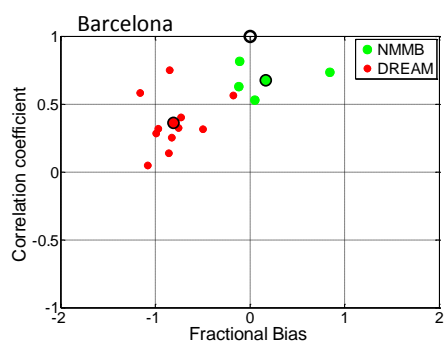
(a)

600



(b)

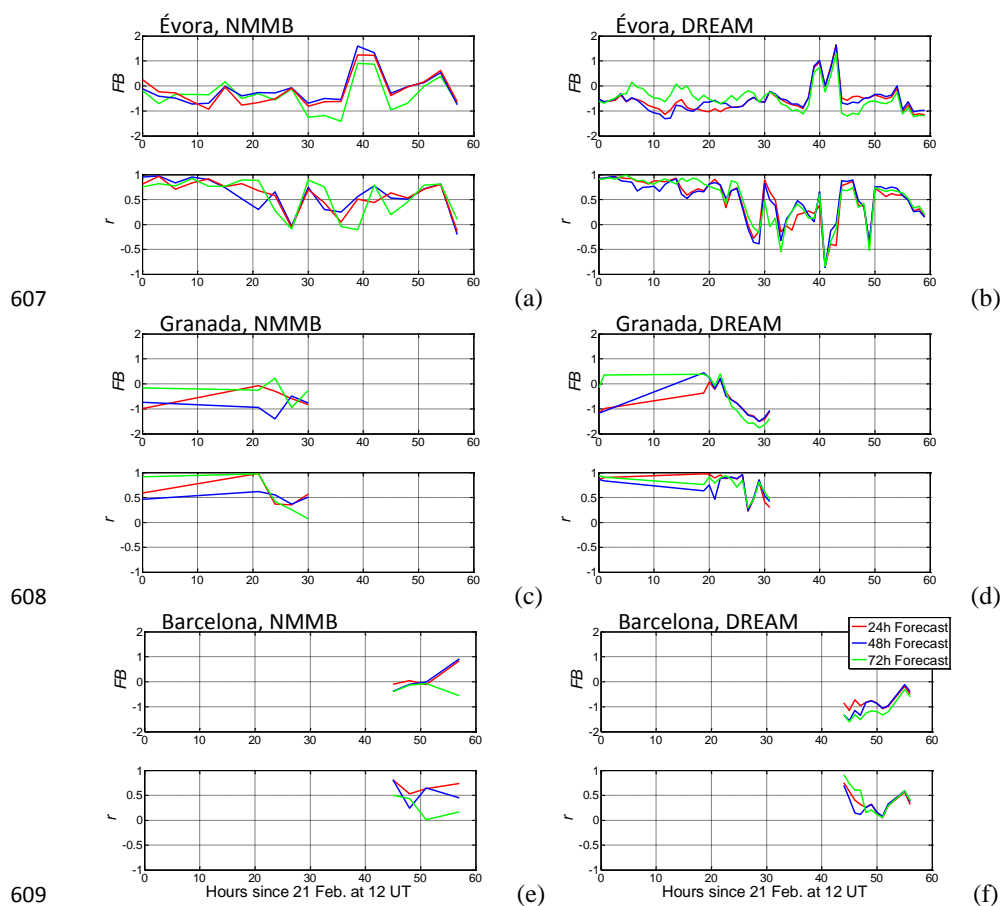
601



(c)

602 **Fig. 14. Correlation coefficient vs. fractional bias calculated for each individual**
 603 **profile in (a) Évora, (b) Granada and (c) Barcelona. All model forecasts are for a**
 604 **lead time of 24 h. The mean values are represented by larger dots edged by a black**
 605 **line. The ideal (FB/r) pair, (0/1), is indicated by a black circle.**

606



607
608
609
610 **Fig. 15. Correlation coefficient and fractional bias vs. time for forecast lead times**
611 **of 24, 48 and 72 h for NMMB/BSC-Dust in (a) Évora, (c) Granada and (e)**
612 **Barcelona and for BSC-DREAM8b in (b) Évora, (d) Granada and (f) Barcelona.**
613 **The legend shown in the last plot applies to all plots.**

614
615
616
617
618
619

620 **Table 5. Main results of the comparison between models and observations.**

Évora (21 Feb. 12UT – 23 Feb. 23UT)						
	NMMB/BSC-Dust			BSC-DREAM8b		
Number of profiles	20			60		
Lead time (hours)	24	48	72	24	48	72
<i>FB</i> (%)	-18.7	-13.5	-36.8	-56.5	-55.7	-49.3
<i>r</i>	0.58	0.59	0.57	0.50	0.51	0.52
Model CoM (km)	2.70	2.8	3.04	2.21	2.27	2.38
Lidar CoM (km)	2.44			2.44		
Granada (21 Feb. 12UT – 22 Feb. 19UT)						
	NMMB/BSC-Dust			BSC-DREAM8b		
Number of profiles	5			15		
Lead time (hours)	24	48	72	24	48	72
<i>FB</i> (%)	-55.5	-86.8	-27.6	-78.0	-72.9	-69.1
<i>r</i>	0.57	0.50	0.53	0.76	0.71	0.75
Model CoM (km)	2.26	2.38	2.14	2.71	2.83	3.07
Lidar CoM (km)	2.88			3.07		
Barcelona (23 Feb. 08UT – 23 Feb. 21UT)						
	NMMB/BSC-Dust			BSC-DREAM8b		
Number of profiles	4			11		
Lead time (hours)	24	48	72	24	48	72
<i>FB</i> (%)	+16.8	+10.6	-29.5	-80.8	-94.3	-116.6
<i>r</i>	0.68	0.54	0.28	0.36	0.32	0.42
Model CoM (km)	3.60	3.72	4.37	2.49	2.49	2.65
Lidar CoM (km)	2.62			2.53		



621 When looking at the temporal mean profiles of extinction coefficient (Fig. 13), the most
622 striking feature is the general large underestimation of BSC-DREAM8b at all heights
623 independently of the site. This underestimation is smaller in Évora, closer to the dust
624 source than Barcelona, where the underestimation is larger. The mean *FB* is actually
625 decreasing from -56.5 % in Évora and -78.0 % in Granada to -80.8 % in Barcelona
626 (Table 5). In Fig. 14 it is observed a horizontal spread of the variability of *FB* larger in
627 Évora and Granada ([-150; 0 %]) than in Barcelona ([-110; -50 %]) probably due to the
628 smaller amount of vertical profiles available in Barcelona. NMMB/BSC-Dust forecasts
629 show a rather good agreement with the observations, especially in Évora. While the
630 model tends to underestimate the observations in Évora (especially below the CoM; the
631 mean *FB* is -18.7 %) and in Granada (especially near the CoM; the mean *FB* is -55.5
632 %), it tends to overestimate the observations in Barcelona (especially above 1 km; the
633 mean *FB* is +16.8 %). The agreement between NMMB/BSC-Dust and the Évora lidar
634 is remarkably good (Fig. 13a), taking into account the atmospheric variability
635 represented by the lidar error bars and the rather long period considered (60 hours).
636 While the NMMB/BSC-Dust profiles reach zero at an approximate height of 5 km in
637 Évora and Granada (similarly to the observations), the profiles in Barcelona start
638 decreasing linearly from $\sim 100 \text{ Mm}^{-1}$ at 5 km height to $\sim 50 \text{ Mm}^{-1}$ at 7 km (when the
639 observations indicate an extinction coefficient lower than 50 Mm^{-1} above 4.5 km and
640 reaching zero at 6 km). Possible explanations of the differences observed between
641 NMMB/BSC-Dust and the observation in Barcelona in the upper part of the profile are
642 given in the next paragraph. Also in Barcelona the lidar profiles show a layer connected
643 to the surface below 1.5 km, which is not reproduced by either of the models. The main
644 reason is probably the presence of non-dust type particles mixed with the dust detected
645 in the observations but not taken into account in the models. It is also worth noting that



646 BSC-DREAM8b reproduces less atmospheric variability than NMMB/BSC-Dust (the
647 red shaded areas are smaller than the green ones), whereas the atmospheric variability
648 denoted by the lidar error bars is large at all sites. This seems to indicate that BSC-
649 DREAM8b has less nervousness than NMMB/BSC-Dust although its time resolution is
650 three times higher.

651 The capacity of the models to reproduce the shape of the dust vertical distribution is
652 estimated with the correlation coefficient calculated between individual modeled and
653 observed profiles. While NMMB/BSC-Dust r values are more or less of the same order
654 of magnitude at all sites (0.58 in Évora, 0.57 in Granada and 0.68 in Barcelona; see
655 Table 6), BSC-DREAM8b r values are more heterogeneous (0.50 in Évora, 0.76 in
656 Granada and 0.36 in Barcelona). The low r value obtained with BSC-DREAM8b in
657 Barcelona (0.36) is apparently due to a vertical downward transport forecast by the
658 model and not visible from the observations (the peak of BSC-DREAM8b profile is
659 approximately 2 km lower than the peak of the lidar, see Fig. 13f). (Huneeus, Basart et
660 al. 2016), who compared NMMB/BSC-Dust and BSC-DREAM8b, among other
661 models, to CALIOP (Cloud Aerosol Lidar with Orthogonal Polarization) profiles during
662 an intense dust outbreak in April 2011 with an AOD \sim 0.8, found a general
663 underestimation of the dust layer height, that was attributed to an overestimation of the
664 dust deposition near the source. The fact that the cloud of points along the r -axis is
665 spreader in Évora (Fig. 13a) than in Granada or Barcelona (Fig. 13b and c) is probably
666 due to the longer time series available in Évora covering two and a half days of the
667 event. Another indicator of the score of the models related to the vertical structure of
668 the dust layer is the center of mass. In general both models retrieve relatively well the
669 center of mass of the dust layers (see Table 5). Leaving apart the center of mass
670 retrieved by NMMB/BSC-Dust in Barcelona, the largest discrepancy between



671 NMMB/BSC-Dust and the observations is: 0.62 km (2.26 vs. 2.88 km); while the
672 largest discrepancy between BSC-DREAM8b and the observations is: 0.36 km (2.71 vs.
673 3.07 km), both of them obtained in Granada. The latter result for BSC-DREAM8b is in
674 complete agreement with the difference of 0.3 ± 1.0 km found between the same model
675 and the EARLINET station of Potenza, Italy, over a period of 12 years and for dust
676 events with AOD < 0.9 (Mona, Papagiannopoulos et al. 2014). In Barcelona, the mean
677 CoM forecasted by NMMB/BSC-Dust is 3.60 km while the lidar measured a mean
678 value of 2.62 km. This large difference is due to the mean NMMB/BSC-Dust profile of
679 extinction in Barcelona which does not reach zero at ~5 km, unlike at the other sites
680 (Fig. 13e; see also the former paragraph). This finding suggests that one or several
681 processes taken into account in NMMB/BSC-Dust and inducing vertical motion of the
682 dust layers did actually not occur. One of these processes is the troposphere–
683 stratosphere exchanges which in some cases has been found to be overestimated by the
684 model because of a misrepresentation of the tropopause that normally limits the
685 maximum altitude of dust transport (Janjic 1994). However, given the limited vertical
686 extension of the dust plume (< 5 km), such an explanation is very unlikely. In our case
687 the vertical upward transport of the dust layers at high altitudes forecast in Barcelona
688 but not in the southern sites is probably due to a too long aerosol lifetime in the upper
689 layers and/or underestimated deposition processes (Mona, Papagiannopoulos et al.
690 2014). Interestingly this overestimation of NMMB/BSC-Dust in the upper layers was
691 also observed by (Biniotoglou, Basart et al. 2015) who found a slight overestimation of
692 NMMB/BSC-Dust above 4.5-5 km when comparing the model with LIRIC
693 (Lidar/Radiometer Inversion Code) profiles of mass concentration at several sites in
694 Europe and by (Sicard, D'Amico et al. 2015) who compared the model with profiles



695 from EARLINET stations during a moderate dust event affecting the western
696 Mediterranean Basin in July 2012.

697 5.2 Forecast skill temporal evolution and comparison for different lead times

698 The temporal evolution of the score of the models (in terms of FB and r) for different
699 lead times shown in Fig. 15 allows to evaluate the forecast skill of each model as a
700 function of time since the forecast initialization. The start of the time series is fixed on
701 21 February, 2017, at 12 UTC, referred in the following as time T_0 , when the first
702 observations are available (in Évora and Granada). The observations available allow to
703 have 60 continuous hours of comparison from the 21st at 12 UTC until the 23rd at 23
704 UTC in Évora; 13 continuous hours of comparison on the 22nd between 07 and 19 UTC
705 in Granada; and 11 quasi-continuous hours of comparison on the 23rd between 08 and
706 21 UTC in Barcelona. In all plots we have represented the temporal evolution of FB
707 and r for lead times of 24, 48 and 72 h. We first discuss the forecast skill temporal
708 evolution for a lead time of 24 h, and then compare it to the evolution at 48 and 72
709 hours.

710 In Évora during the first 20 hours (Fig. 15a and b, red lines) both models have similar
711 and more or less stable correlation coefficients with values larger than 0.5. The
712 fractional bias is negative and varies in the range $[-100; 0 \text{ \%}]$. It is larger (in absolute
713 value) for BSC-DREAM8b than for NNMB/BSC-Dust. At $T_0 + 20$ hours (the 22nd at 08
714 UTC) the situation starts to degrade: FB variations are larger from one prognostic to
715 the next, especially for NNMB/BSC-Dust, and r passes regularly below the value of
716 0.5. A few hours before $T_0 + 40$ hours (the 23rd at 04 UTC) and only for a period of 5-6
717 hours both models overestimate the extinction coefficient ($+50 < FB < +150 \text{ \%}$). During
718 the first hours of the 23rd the AOD in Évora reached its highest values (~ 2.5 ; see Fig. 3).



719 In that sense, it seems that the peak of the event is well reproduced in time by the
720 models but its intensity is overestimated. In Granada (Fig. 15c and d, red lines) the
721 prognostic of NNMB/BSC-Dust is quantitatively better (smaller values of FB) but
722 qualitatively worst (smaller correlation coefficients) than for BSC-DREAM8b. Our
723 findings in Granada are in the same line as those found by (Sicard, D'Amico et al. 2015)
724 for a moderate dust event affecting the western Mediterranean Basin in July 2012 who
725 also found that NNMB/BSC-Dust reproduced quantitatively better the profiles while
726 BSC-DREAM8b reproduced better the shape of the profiles. However in the intense
727 event described in this study, both models have better prognostics (mean $FB > -100\%$;
728 mean $r > 0.5$, see Fig. 14b) than in (Sicard, D'Amico et al. 2015) ($FB < -100\%$; $r < 0.2$).
729 The decrease of FB visible for both models in Granada and starting at $T_0 + 20$ (the 22nd
730 at 08 UTC) coincides with the increase of AOD from ~ 0.5 to values above 2.0 (see Fig.
731 3). While on the peak day in Évora (the 23rd) both prognostics show an overestimation
732 for a short period of time, on the peak day in Granada (the 22nd) the general
733 underestimation of both prognostics is accentuated, especially for BSC-DREAM8b. In
734 Barcelona (Fig. 15 e and f, red lines) the comparison starts at $T_0 + 44$ (the 23rd at 08
735 UTC) at the peak of the event in Barcelona (AOD > 2.0, see Fig. 3). NNMB/BSC-Dust
736 shows a very good quantitative agreement in the morning and an overestimation in the
737 afternoon, while BSC-DREAM8b shows an underestimation, which decreases with
738 time. The shape of the vertical profiles is better reproduced by NNMB/BSC-Dust (
739 $r > 0.5$) than by BSC-DREAM8b ($r < 0.5$). In general the forecast skills of BSC-
740 DREAM8b in Barcelona are not as good as those of the southernmost sites. This
741 difference, also observed by (Huneeus, Basart et al. 2016) for dust northward transport,
742 might be explained by the difficulties of the models in simulating horizontal winds and
743 vertical dust propagation.



744 If we now look at the forecast skill as a function of lead time, i.e. at the differences
745 between the red, blue and green lines in Fig. 15, corresponding, respectively, to lead
746 times of 24, 48 and 72 hours, the most striking result is that, at first sight, no clear
747 degradation of the prognostics is clearly visible. There is a difference in the temporal
748 evolution of the prognostics: the prognostics at 24 and 48 h are usually quite similar and
749 the one at 72 h is the one that differs the most from the prognostic at 24 h; but all in all,
750 for Évora and Granada, the two stations closest to the source, if one looks at the overall
751 mean values in Table 6, no clear tendency appears neither in terms of FB , nor r . In
752 this sense these results are in agreement with those of (Huneus, Basart et al. 2016) who
753 found that the forecast skill of both models for AOD was independent of the forecasting
754 lead time in the domain they defined as southern Europe. In Barcelona a slight
755 degradation of the model scores occurs with increasing lead times: the fractional bias
756 increases (in absolute value; both models) and the correlation coefficient decreases
757 (NMMB/BSC-Dust) between the prognostics at 24 and 72 h. This deterioration of the
758 forecast skills is not observed in (Huneus, Basart et al. 2016) and may be due to the
759 singularity and exceptionality of the event described in our study.

760 **6 Conclusions**

761

762 An extreme dust outbreak transported from Northern Africa to the western
763 Mediterranean during 20-23 February 2017 has been reported and analyzed in the IP.
764 By means of lidar and sun-photometer measurements, we have provided a
765 representative picture of this extreme event by means of a detailed 4-D characterization
766 of aerosol optical properties and their evolution during the African event. Furthermore,
767 the combined use of active and passive remote sensing instruments along with dust
768 models has provided useful information to better understand the complexity of dust



769 long-range transport, its extreme character and also the capability of dust models to
770 forecast such events.

771 The appearance of the Moroccan low reinforced by the Atlantic anticyclonic system was
772 responsible for the tropospheric flow that advected atmospheric mineral dust over the IP
773 during this extreme event. The southern stations were affected earlier (Granada, Évora
774 and Cabo da Roca) than northern stations (Burjassot, Madrid and Barcelona) as the first
775 were closer to the dust source. From the photometry, we would like to remark two main
776 ideas concerning the most intense stages of the event. Firstly, AOD at 675 nm were
777 registered to be around and over 2, the Ångström Exponent (440/870 nm) was close to
778 0, and SSA was close to 1 in most of AERONET stations, which indicates an
779 extraordinarily high aerosol load, a large aerosol size and the dispersive nature of these
780 particles, characteristics that are attributed to mineral dust. Secondly, the African dust
781 outbreak was accompanied by the presence of clouds that hampered an adequate
782 retrieval and consequently no sun-photometer observations were available at some
783 AERONET stations.

784 From lidar measurements, the African dust plume could be observed in each lidar
785 station. In general, the altitude range of the plume was observed from the ground until
786 4-5 km asl approximately at every lidar station. Maximum values of backscatter
787 coefficients at 532 nm were registered by each lidar system in the range $1 - 1.5 \cdot 10^{-5} \text{ m}^{-1}$
788 sr^{-1} , where, during the most intense stages the high aerosol load prevented the retrieval,
789 which could not be carried out. This is an issue that also complicated the retrieval in
790 every site. Minimum backscatter-related Ångström exponents at these stages were
791 monitored very close to 0, which are in agreement with the results provided by the
792 sunphotometry. Lidar ratios were found in the range 40 - 55 sr at 355 nm and 34 - 61 sr
793 at 532 nm during the event at Évora and Granada. Particle and volume depolarization



794 ratios, registered at those stations where depolarizing channels were available, have
795 shown an interesting consistency of these values given the fact they were very similar.
796 In general, large particle and volume depolarization ratios are attributed to mineral dust
797 since they are not spherical particles and produce a higher backscatter signal related to
798 the cross-polarized component. The larger the particle and volume depolarization ratios,
799 the purer mineral dust. Likewise, according to these depolarizing properties, lidar
800 systems equipped with this channel have indicated perfectly the different structures and
801 aerosol layers throughout the vertical column to distinguish local aerosol from mineral
802 aerosol for instance in Granada. These findings suggest the need of use of combined
803 instrumentation to characterize adequately aerosol optical properties during this kind of
804 events.

805 When it comes to forecasting this extreme event, two dust models have been used:
806 BSC-DREAM8b and NMMB/BSC-Dust. According to the fractional bias and the
807 correlation coefficient analysis there is a large underestimation ($FB < -56.5\%$ for a
808 lead time of 24 h) in the forecast of the extinction coefficient provided by BSC-
809 DREAM8b at all heights independently of the site. By contrast, NMMB/BSC-Dust
810 forecasts presented a better agreement with the observations, especially in Évora ($FB =$
811 -18.7% ; $r = 0.58$ for a lead time of 24 h;). However the NMMB/BSC-Dust reproduced
812 a higher atmospheric variability than BSC-DREAM8b. Some discrepancies such as the
813 forecast of dust by NMMB/BSC-Dust in layers well above 5 km are still not completely
814 understood and further research is needed. Finally, with regard to the forecast skill as a
815 function of lead time of each model, no clear degradation of the prognostic is
816 appreciated at 24, 48 and 72h for Évora and Granada stations, however it does for
817 Barcelona, which is in principle attributed to the singularity of the event.

818



819 **Acknowledgments**

820 The research leading to these results has received funding from ACTRIS-2-H2020
821 (grant agreement no. 654109) and also from the MINECO (Spanish Ministry of
822 Industry, Economy and Competitiveness) under projects: PROACLIM (CGL2014-
823 52877-R), CRISOL (CGL2017-85344-R), CGL2013-45410-R, CGL2016-81092-R and
824 grant TEC2015-63832-P. Co-funding was also provided by the European Union through
825 the European Regional Development Fund, included in the COMPETE 2020
826 (Operational Program Competitiveness and Internationalization) through the ICT
827 project (UID/GEO/04683/2013) with the reference POCI-01-0145-FEDER-007690 and
828 also through ALOP (ALT20-03-0145-FEDER-000004) and DNI-A (ALT20-03-0145-
829 FEDER-000011) projects. This work has also been funded by the research project
830 “Evaluación del impacto en la salud de eventos atmosféricos extremos producidos por el
831 cambio climático” (SINERGIA) and the “Fundación Biodiversidad”, from the Spanish
832 Ministry of Agriculture and Fisheries, Food & Environment (MAPAMA).
833 Measurements in Barcelona were also supported by the European Fund for Regional
834 Development and the Unidad de Excelencia María de Maeztu (grant MDM-2016-0600)
835 funded by the Agencia Estatal de Investigación, Spain. The authors express gratitude to
836 the Juan de la Cierva-Formación program (grant FJCI-2015-23904) for the support
837 provided. This work was supported by the Andalusia Regional Government through
838 project P12-RNM-2409 as well, and by the University of Granada through “Plan
839 Propio. Programa 9 Convocatoria 2013”. The authors thankfully acknowledge the
840 FEDER program for the instrumentation used in this work. We thank AERONET and
841 Juan Ramón Moreta González, Jose M. Baldasano, Ana Maria Silva, José Antonio
842 Martínez for their effort in establishing and maintaining the Madrid, Barcelona, Évora,
843 Burjassot site, respectively. The authors thank S. Basart and O. Jorba from the Dept. of



844 Earth Sciences of the Barcelona Supercomputing Center for providing the dust model
845 data.

846 **References.**

847 Amiridis, V., D. Balis, E. Giannakaki, A. Stohl, S. Kazadzis, M. Koukoulis and P. Zanis (2009).
848 "Optical characteristics of biomass burning aerosols over Southeastern Europe determined
849 from UV-Raman lidar measurements." Atmospheric Chemistry and Physics **9**(7): 2431-2440.

850

851 Andreae, M. (1995). "Climate effects of changing atmospheric aerosol levels. In: Henderson-
852 Sellers, A. (Ed), World Survey of Climatology, 16, Future Climate of the World. Elsevier, New
853 York, pp. 341-392."

854

855 Ångström, A. (1964). "THE PARAMETERS OF ATMOSPHERIC TURBIDITY." Tellus **16**(1): 64-75.

856 Ansmann, A., I. Mattis, D. Müller, U. Wandinger, M. Radlach, D. Althausen and R. Damoah
857 (2005). "Ice formation in Saharan dust over central Europe observed with
858 temperature/humidity/aerosol Raman lidar." Journal of Geophysical Research: Atmospheres
859 **110**(D18).

860

861 Ansmann, A., F. Rittmeister, R. Engelmann, S. Basart, O. Jorba, C. Spyrou, S. Rémy, A. Skupin, H.
862 Baars and P. Seifert (2017). "Profiling of Saharan dust from the Caribbean to western Africa–
863 Part 2: Shipborne lidar measurements versus forecasts." Atmospheric Chemistry and Physics
864 **17**(24): 14987-15006.

865

866 Ansmann, A., U. Wandinger, M. Riebesell, C. Weitkamp and W. Michaelis (1992). "Independent
867 measurement of extinction and backscatter profiles in cirrus clouds by using a combined
868 Raman elastic-backscatter lidar." Applied Optics **31**(33): 7113-7131.

869

870 Basart, S., C. Perez, S. Nickovic, E. Cuevas and J. Baldasano (2012). "Development and
871 evaluation of the BSC-DREAM8b dust regional model over Northern Africa, the Mediterranean
872 and the Middle East." Tellus Series B-Chemical and Physical Meteorology **64**.

873

874 Binietoglou, I., S. Basart, L. Alados-Arboledas, V. Amiridis, A. Argyrouli, H. Baars, J. Baldasano,
875 D. Balis, L. Belegante, J. Bravo-Aranda, P. Burlizzi, V. Carrasco, A. Chaikovskiy, A. Comeron, G.
876 D'Amico, M. Filioglou, M. Granados-Munoz, J. Guerrero-Rascado, L. Ilic, P. Kokkalis, A. Maurizi,
877 L. Mona, F. Monti, C. Munoz-Porcar, D. Nicolae, A. Papayannis, G. Pappalardo, G. Pejanovic, S.
878 Pereira, M. Perrone, A. Pietruczuk, M. Posyniak, F. Rocadenbosch, A. Rodriguez-Gomez, M.
879 Sicard, N. Siomos, A. Szkop, E. Terradellas, A. Tsekeri, A. Vukovic, U. Wandinger and J. Wagner
880 (2015). "A methodology for investigating dust model performance using synergistic
881 EARLINET/AERONET dust concentration retrievals." Atmospheric Measurement Techniques
882 **8**(9): 3577-3600.

883

884 Boucher, O., Randall, D., Artaxo, P., Bretherton, C., Feingold, G., P. Forster, Kerminen, V.-M.,
885 Kondo, Y., Liao, H., Lohmann, U., P. Rasch, Satheesh, S. K., Sherwood, S., Stevens, B., and
886 Zhang, J. X. Y.; edited by: Stocker, T. F., Qin, D., Plattner, G.-K., Tignor, A. M., S. K., Boschung,
887 J., Nauels, A., Xia, Y., Bex, V., and P. M. and Midgley (2013). Clouds and Aerosols. Climate
888 Change 2013: The Physical Science Basis. Cambridge, United Kingdom and New York, NY, USA:
889 571–657.

890

891 Cazorla, A., J. A. Casquero-Vera, R. Román, J. L. Guerrero-Rascado, C. Toledano, V. E. Cachorro,
892 J. A. G. Orza, M. L. Cancillo, A. Serrano, G. Titos, M. Pandolfi, A. Alastuey, N. Hanrieder and L.



- 893 Alados-Arboledas (2017). "Near real time processing of ceilometer network data:
894 characterizing an extraordinary dust outbreak over the Iberian Peninsula." Atmos. Chem. Phys.
895 Discuss. **2017**: 1-28.
- 896
- 897 Cuevas, E., A. J. Gómez-Peláez, S. Rodríguez, E. Terradellas, S. Basart, R. D. Garcia, O. E. Garcia
898 and S. Alonso-Perez (2017). "The pulsating nature of large-scale Saharan dust transport as a
899 result of interplays between mid-latitude Rossby waves and the North African Dipole
900 Intensity." Atmospheric Environment **167**: 586-602.
- 901
- 902 Díaz, J., C. Linares, R. Carmona, A. Russo, C. Ortiz, P. Salvador and R. M. Trigo (2017). "Saharan
903 dust intrusions in Spain: health impacts and associated synoptic conditions." Environmental
904 research **156**: 455-467.
- 905
- 906 Fernald, F. G. (1984). "Analysis of Atmospheric Lidar Observations - Some Comments." Applied
907 Optics **23**(5): 652-653.
- 908
- 909 Forster, P., V. Ramaswamy, P. Artaxo, T. Berntsen, R. Betts, D. Fahey, J. Haywood, J. Lean, D.
910 Lowe, G. Myhre, J. Nganga, G. Prinn, G. Raga, M. Schulz and R. Van Dorland (2007). "Changes in
911 atmospheric constituents and in radiative forcing." Climate Change 2007: The physical Science
912 Basis, 129-234, Cambridge Univ. Press, U.K.
- 913
- 914 Gobbi, G., F. Angelini, F. Barnaba, F. Costabile, J. Baldasano, S. Basart, R. Sozzi and A. Bolignano
915 (2013). "Changes in particulate matter physical properties during Saharan advections over
916 Rome (Italy): a four-year study, 2001-2004." Atmospheric Chemistry and Physics **13**(15): 7395-
917 7404.
- 918
- 919 Guerrero-Rascado, J., F. Olmo, I. Aviles-Rodriguez, F. Navas-Guzman, D. Perez-Ramirez, H.
920 Lyamani and L. Arboledas (2009). "Extreme Saharan dust event over the southern Iberian
921 Peninsula in september 2007: active and passive remote sensing from surface and satellite."
922 Atmospheric Chemistry and Physics **9**(21): 8453-8469.
- 923
- 924 Guerrero-Rascado, J., B. Ruiz and L. Alados-Arboledas (2008). "Multi-spectral Lidar
925 characterization of the vertical structure of Saharan dust aerosol over southern Spain."
926 Atmospheric Environment **42**(11): 2668-2681.
- 927
- 928 Holben, B., T. Eck, I. Slutsker, D. Tanre, J. Buis, A. Setzer, E. Vermote, J. Reagan, Y. Kaufman, T.
929 Nakajima, F. Lavenu, I. Jankowiak and A. Smirnov (1998). "AERONET - A federated instrument
930 network and data archive for aerosol characterization." Remote Sensing of Environment **66**(1):
931 1-16.
- 932
- 933 Holben, B., D. Tanre, A. Smirnov, T. Eck, I. Slutsker, N. Abuhassan, W. Newcomb, J. Schafer, B.
934 Chatenet, F. Lavenu, Y. Kaufman, J. Castle, A. Setzer, B. Markham, D. Clark, R. Frouin, R.
935 Halthore, A. Karneli, N. O'Neill, C. Pietras, R. Pinker, K. Voss and G. Zibordi (2001). "An
936 emerging ground-based aerosol climatology: Aerosol optical depth from AERONET." Journal of
937 Geophysical Research-Atmospheres **106**(D11): 12067-12097.
- 938
- 939 Huneus, N., S. Basart, S. Fiedler, J.-J. Morcrette, A. Benedetti, J. Mulcahy, E. Terradellas, C. P.
940 Garcia-Pando, G. Pejanovic and S. Nickovic (2016). "Forecasting the northern African dust
941 outbreak towards Europe in April 2011: a model intercomparison." Atmospheric chemistry and
942 physics **16**(8): 4967.
- 943



- 944 IPCC (2013). "Summary for Policymakers. In: Climate Change 2013: The Physical Science Basis.
945 Contribution of Working Group I to the Fifth Assessment Report of the Intergovernmental
946 Panel on Climate Change, edited by Stocker, T.F., D. Qin, G.-K. Plattner, M. Tignor, S.K. Allen, J.
947 Boschung, A. Nauels, Y. Xia, V. Bex and P.M. Midgley. Cambridge University Press, Cambridge,
948 United Kingdom and New York, NY, USA.".
- 949
950 Janjic, Z. (1994). "THE STEP-MOUNTAIN ETA COORDINATE MODEL - FURTHER DEVELOPMENTS
951 OF THE CONVECTION, VISCOUS SUBLAYER, AND TURBULENCE CLOSURE SCHEMES." Monthly
952 Weather Review **122**(5): 927-945.
- 953
954 Klein, H., S. Nickovic, W. Haunold, U. Bundke, B. Nillius, M. Ebert, S. Weinbruch, L. Schuetz, Z.
955 Levin and L. A. Barrie (2010). "Saharan dust and ice nuclei over Central Europe." Atmospheric
956 Chemistry and Physics **10**(21): 10211-10221.
- 957
958 Klett, J. D. (1981). "Stable Analytical Inversion Solution for Processing Lidar Returns." Applied
959 Optics **20**(2): 211-220.
- 960
961 Lafontaine, C., R. Bryson and W. Wendland (1990). "AIRSTREAM REGIONS OF NORTH-AFRICA
962 AND THE MEDITERRANEAN." Journal of Climate **3**(3): 366-372.
- 963
964 Mahowald, N., A. Baker, G. Bergametti, N. Brooks, R. Duce, T. Jickells, N. Kubilay, J. Prospero
965 and I. Tegen (2005). "Atmospheric global dust cycle and iron inputs to the ocean." Global
966 Biogeochemical Cycles **19**(4).
- 967
968 Mamouri, R., A. Ansmann, A. Nisantzi, P. Kokkalis, A. Schwarz and D. Hadjimitsis (2013). "Low
969 Arabian dust extinction-to-backscatter ratio." Geophysical Research Letters **40**(17): 4762-4766.
970 Mamouri, R., A. Ansmann, A. Nisantzi, S. Solomos, G. Kallos and D. Hadjimitsis (2016).
971 "Extreme dust storm over the eastern Mediterranean in September 2015: satellite, lidar, and
972 surface observations in the Cyprus region." Atmospheric Chemistry and Physics **16**(21): 13711-
973 13724.
- 974
975 Mona, L., A. Amodeo, M. Pandolfi and G. Pappalardo (2006). "Saharan dust intrusions in the
976 Mediterranean area: Three years of Raman lidar measurements." Journal of Geophysical
977 Research-Atmospheres **111**(D16).
- 978
979 Mona, L., N. Papagiannopoulos, S. Basart, J. Baldasano, I. Biniotoglou, C. Cornacchia and G.
980 Pappalardo (2014). "EARLINET dust observations vs. BSC-DREAM8b modeled profiles: 12-year-
981 long systematic comparison at Potenza, Italy." Atmospheric Chemistry and Physics **14**(16):
982 8781-8793.
- 983
984 Muller, D., A. Ansmann, V. Freudenthaler, K. Kandler, C. Toledano, A. Hiebsch, J. Gasteiger, M.
985 Esselborn, M. Tesche, B. Heese, D. Althausen, B. Weinzierl, A. Petzold and W. von Hoyningen-
986 Huene (2010). "Mineral dust observed with AERONET Sun photometer, Raman lidar, and in situ
987 instruments during SAMUM 2006: Shape-dependent particle properties." Journal of
988 Geophysical Research-Atmospheres **115**.
- 989
990 Muller, D., B. Heinold, M. Tesche, I. Tegen, D. Althausen, L. Arboledas, V. Amiridis, A. Amodeo,
991 A. Ansmann and D. Balis (2009). "EARLINET observations of the 14-22-May long-range dust
992 transport event during SAMUM 2006: validation of results from dust transport modelling."
993 TELLUS. SERIES B, CHEMICAL AND PHYSICAL METEOROLOGY **61**(1): 325-339.
- 994



- 995 Nisantzi, A., R. Mamouri, A. Ansmann, G. Schuster and D. Hadjimitsis (2015). "Middle East
996 versus Saharan dust extinction-to-backscatter ratios." Atmospheric Chemistry and Physics
997 **15**(12): 7071-7084.
- 998
999 Obregón, M., S. Pereira, V. Salgueiro, M. J. Costa, A. M. Silva, A. Serrano and D. Bortoli (2015).
1000 "Aerosol radiative effects during two desert dust events in August 2012 over the Southwestern
1001 Iberian Peninsula." Atmospheric Research **153**: 404-415.
- 1002
1003 Pappalardo, G., A. Amodeo, A. Apituley, A. Comeron, V. Freudenthaler, H. Linne, A. Ansmann,
1004 J. Bosenberg, G. D'Amico, I. Mattis, L. Mona, U. Wandinger, V. Amiridis, L. Alados-Arboledas, D.
1005 Nicolae and M. Wiegner (2014). "EARLINET: towards an advanced sustainable European
1006 aerosol lidar network." Atmospheric Measurement Techniques **7**(8): 2389-2409.
- 1007
1008 Pappalardo, G., A. Amodeo, M. Pandolfi, U. Wandinger, A. Ansmann, J. Bosenberg, V. Matthias,
1009 V. Amiridis, F. De Tomasi, M. Frioud, M. Iarlori, L. Komguem, A. Papayannis, F. Rocadenbosch
1010 and X. Wang (2004). "Aerosol lidar intercomparison in the framework of the EARLINET project.
1011 3. Raman lidar algorithm for aerosol extinction, backscatter, and lidar ratio." Applied Optics
1012 **43**(28): 5370-5385.
- 1013 Perez, C., K. Hausteiner, Z. Janjic, O. Jorba, N. Huneus, J. Baldasano, T. Black, S. Basart, S.
1014 Nickovic, R. Miller, J. Perlwitz, M. Schulz and M. Thomson (2011). "Atmospheric dust modeling
1015 from meso to global scales with the online NMMB/BSC-Dust model - Part 1: Model description,
1016 annual simulations and evaluation." Atmospheric Chemistry and Physics **11**(24): 13001-13027.
- 1017 Perez, C., S. Nickovic, G. Pejanovic, J. Baldasano and E. Ozsoy (2006). "Interactive dust-
1018 radiation modeling: A step to improve weather forecasts." Journal of Geophysical Research-
1019 Atmospheres **111**(D16).
- 1020
1021 Pey, J., X. Querol, A. Alastuey, F. Forastiere and M. Stafoggia (2013). "African dust outbreaks
1022 over the Mediterranean Basin during 2001–2011: PM 10 concentrations, phenomenology and
1023 trends, and its relation with synoptic and mesoscale meteorology." Atmospheric Chemistry
1024 and Physics **13**(3): 1395-1410.
- 1025
1026 Preissler, J., F. Wagner, S. Pereira and J. Guerrero-Rascado (2011). "Multi-instrumental
1027 observation of an exceptionally strong Saharan dust outbreak over Portugal." Journal of
1028 Geophysical Research-Atmospheres **116**.
- 1029
1030 Prospero, J., P. Ginoux, O. Torres, S. Nicholson and T. Gill (2002). "Environmental
1031 characterization of global sources of atmospheric soil dust identified with the Nimbus 7 Total
1032 Ozone Mapping Spectrometer (TOMS) absorbing aerosol product." Reviews of Geophysics
1033 **40**(1).
- 1034
1035 Querol, X., J. Pey, M. Pandolfi, A. Alastuey, M. Cusack, N. Pérez, T. Moreno, M. Viana, N.
1036 Mihalopoulos and G. Kallos (2009). "African dust contributions to mean ambient PM₁₀ mass-
1037 levels across the Mediterranean Basin." Atmospheric Environment **43**(28): 4266-4277.
- 1038
1039 Salvador, P., S. M. Almeida, J. Cardoso, M. Almeida-Silva, T. Nunes, M. Cerqueira, C. Alves, M.
1040 A. Reis, P. C. Chaves, B. Artinano and C. Pio (2016). "Composition and origin of PM₁₀ in Cape
1041 Verde: Characterization of long-range transport episodes." Atmospheric Environment **127**:
1042 326-339.
- 1043
1044 Salvador, P., S. Alonso-Perez, J. Pey, B. Artinano, J. de Bustos, A. Alastuey and X. Querol (2014).
1045 "African dust outbreaks over the western Mediterranean Basin: 11-year characterization of



- 1046 atmospheric circulation patterns and dust source areas." Atmospheric Chemistry and Physics
1047 **14**(13): 6759-6775.
- 1048
- 1049 Salvador, P., B. Artñano, F. Molero, M. Viana, J. Pey, A. Alastuey and X. Querol (2013). "African
1050 dust contribution to ambient aerosol levels across central Spain: Characterization of long-
1051 range transport episodes of desert dust." Atmospheric Research **127**: 117-129.
- 1052
- 1053 Santos, D., M. J. Costa, A. M. Silva and R. Salgado (2013). "Modeling Saharan desert dust
1054 radiative effects on clouds." Atmospheric research **127**: 178-194.
- 1055
- 1056 Sicard, M., R. Barragan, F. Dulac, L. Alados-Arboledas and M. Mallet (2016). "Aerosol optical,
1057 microphysical and radiative properties at regional background insular sites in the western
1058 Mediterranean." Atmospheric Chemistry and Physics **16**(18): 12177-12203.
- 1059
- 1060 Sicard, M., G. D'Amico, A. Comeron, L. Mona, L. Alados-Arboledas, A. Amodeo, H. Baars, J.
1061 Baldasano, L. Belegante, I. Biniotoglou, J. Bravo-Aranda, A. Fernandez, P. Freville, D. Garcia-
1062 Vizcaino, A. Giunta, M. Granados-Munoz, J. Guerrero-Rascado, D. Hadjimitsis, A. Haeefe, M.
1063 Hervo, M. Iarlori, P. Kokkalis, D. Lange, R. Mamouri, I. Mattis, F. Molero, N. Montoux, A.
1064 Munoz, C. Porcar, F. Navas-Guzman, D. Nicolae, A. Nisantzi, N. Papagiannopoulos, A.
1065 Papayannis, S. Pereira, J. Preissler, M. Pujadas, V. Rizi, F. Rocadenbosch, K. Sellegri, V.
1066 Simeonov, G. Tsaknakis, F. Wagner and G. Pappalardo (2015). "EARLINET: potential
1067 operationality of a research network." Atmospheric Measurement Techniques **8**(11): 4587-
1068 4613.
- 1069
- 1070 Sorribas, M., J. Adame, E. Andrews and M. Yela (2017). "An anomalous African dust event and
1071 its impact on aerosol radiative forcing on the Southwest Atlantic coast of Europe in February
1072 2016." Science of the Total Environment **583**: 269-279.
- 1073
- 1074 Stafoggia, M., S. Zauli-Sajani, J. Pey, E. Samoli, E. Alessandrini, X. Basagaña, A. Cernigliaro, M.
1075 Chiusolo, M. Demaria and J. Díaz (2016). "Desert dust outbreaks in Southern Europe:
1076 contribution to daily PM10 concentrations and short-term associations with mortality and
1077 hospital admissions." Environmental health perspectives **124**(4): 413.
- 1078
- 1079 Tsekeri, A., A. Lopatin, V. Amiridis, E. Marinou, J. Igloffstein, N. Siomos, S. Solomos, P. Kokkalis,
1080 R. Engelmann and H. Baars (2017). "GARRLiC and LIRIC: strengths and limitations for the
1081 characterization of dust and marine particles along with their mixtures." Atmospheric
1082 Measurement Techniques **10**(12): 4995.
- 1083
- 1084 Wagner, F., D. Bortoli, S. Pereira, M. J. Costa, A. SILVA, B. Weinzierl, M. Esselborn, A. Petzold, K.
1085 Rasp and B. Heinold (2009). "Properties of dust aerosol particles transported to Portugal from
1086 the Sahara desert." Tellus B **61**(1): 297-306.
- 1087
- 1088 Weinzierl, B., A. Ansmann, J. Prospero, D. Althausen, N. Benker, F. Chouza, M. Dollner, D.
1089 Farrell, W. Fomba, V. Freudenthaler, J. Gasteiger, S. Gross, M. Haarig, B. Heinold, K. Kandler, T.
1090 Kristensen, O. Mayol-Bracero, T. Muller, O. Reitebuch, D. Sauer, A. Schafner, K. Schepanski, A.
1091 Spanu, I. Tegen, C. Toledano and A. Walser (2017). "THE SAHARAN AEROSOL LONG-RANGE
1092 TRANSPORT AND AEROSOL-CLOUD-INTERACTION EXPERIMENT Overview and Selected
1093 Highlights." Bulletin of the American Meteorological Society **98**(7): 1427-1451.
- 1094
- 1095 Weinzierl, B., D. Sauer, A. Minikin, O. Reitebuch, F. Dahlkötter, B. Mayer, C. Emde, I. Tegen, J.
1096 Gasteiger, A. Petzold, A. Veira, U. Kueppers and U. Schumann (2012). "On the visibility of



- 1097 airborne volcanic ash and mineral dust from the pilot's perspective in flight." Physics and
1098 Chemistry of the Earth **45-46**: 87-102.
1099
1100 World Meteorological Organization, W. M. O. (2011). "Weather Extreme in a Changing Climate:
1101 Hindsight on Foresight " WMO-No. 1075 (ISBN: 978-92-63-11075-6).
1102